

RSC Advances



This is an *Accepted Manuscript*, which has been through the Royal Society of Chemistry peer review process and has been accepted for publication.

Accepted Manuscripts are published online shortly after acceptance, before technical editing, formatting and proof reading. Using this free service, authors can make their results available to the community, in citable form, before we publish the edited article. This *Accepted Manuscript* will be replaced by the edited, formatted and paginated article as soon as this is available.

You can find more information about *Accepted Manuscripts* in the [Information for Authors](#).

Please note that technical editing may introduce minor changes to the text and/or graphics, which may alter content. The journal's standard [Terms & Conditions](#) and the [Ethical guidelines](#) still apply. In no event shall the Royal Society of Chemistry be held responsible for any errors or omissions in this *Accepted Manuscript* or any consequences arising from the use of any information it contains.

Investigation of plasma electrolytic oxidation on valve metals by means of molecular spectroscopy – A review

Stevan Stojadinović^{a*}, Rastko Vasilic^a, Miljenko Perić^b

^aUniversity of Belgrade, Faculty of Physics, Studentski trg 12–16, 11000 Belgrade, Serbia

^bUniversity of Belgrade, Faculty of Physical Chemistry, Studentski trg 12–16, 11000
Belgrade, Serbia

*Corresponding author. Tel: + 381-11-7158161; Fax: + 381-11-3282619

E-mail address: sstevan@ff.bg.ac.rs (Stevan Stojadinović)

Abstract

A review of results of molecular spectroscopic investigations during plasma electrolytic oxidation of valve metals is presented. Particular attention is paid to three spectral systems, $B^1\Sigma^+ \rightarrow X^1\Sigma^+$ of MgO, and $B^2\Sigma^+ \rightarrow X^2\Sigma^+$, and $C^2\Pi - X^2\Sigma^+$ of AlO. It was shown that a reliable assignment of the observed spectral features can only be carried out by critical comparison with the data obtained in high-resolution spectroscopy, and by using the results of quantum mechanical structure calculations. Assuming the existence of partial local thermal equilibrium, we used our spectroscopic results to determine the plasma temperature. Although limited in quality, the obtained spectra are very rich, they cover large wavelength regions, and are used to obtain information about physical and chemical processes that take place in the course of plasma electrolytic oxidation of light metals and their alloys.

1. INTRODUCTION

In the present study, we review the results of investigations on molecular emission spectra recorded during plasma electrolytic oxidation of magnesium and aluminum. The goal of these investigations was to get information about the processes that take place in our systems, with the aim to become able to monitor them. Here we focus our attention to three spectral systems, $B\ ^1\Sigma^+ \rightarrow X\ ^1\Sigma^+$ of MgO and $B\ ^2\Sigma^+ \rightarrow X\ ^2\Sigma^+$ and $C\ ^2\Pi - X\ ^2\Sigma^+$ of AlO. Random appearance of spectral sources (microdischarge plasmas), poor resolution, low intensities, and unfavorable signal/noise ratios, caused great difficulties in assignment of molecular bands. The assignment was carried out by comparison with the data obtained in high-resolution spectroscopy, but also by using the results of quantum mechanical structure calculations. Assuming the existence of partial local thermal equilibrium, we used our spectroscopic results to determine the plasma temperature.

The paper is organized as follows: After the introductory section, in Section 2 we describe briefly the process of plasma electrolytic oxidation and in Section 3 we give the key information about our experimental setup. In quite extensive Section 4 we present the theoretical background of spectral investigations we carried out. The formulae collected in this section are used to explain the features of recorded spectra. The results for MgO are presented in Section 5 and those for AlO in Section 6. We conclude the paper with Section 7, where we address briefly a model that describes the systems we have been dealing with.

2. PLASMA ELECTROLYTIC OXIDATION

The process, which is the topic of the present study, is based on the anodization of valve metals (aluminum, magnesium, titanium, zirconium, tantalum, etc.) in aqueous solutions at applied potential greater than breakdown voltage (typically from 400 V to 600 V) of the original oxide film. This process is known as plasma electrolytic oxidation (PEO), microarc oxidation (MAO) or anodic spark deposition (ASD). In this work, we will use the terminology plasma electrolytic oxidation, because it has become dominant in the literature.

PEO is an economic, efficient, and environmentally benign processing technique capable of producing in-situ oxide coatings on valve metals, as well as on their alloys. Oxide coatings have controllable morphology and composition, excellent bonding strength with the substrate,

good electrical and thermal properties, high microhardness, high-quality wear and corrosion resistance, etc. The PEO process is coupled with the formation of plasma, as indicated by the presence of microdischarges on the metal surface, accompanied by gas evolution.¹⁻³ The anodic gas consists predominantly of oxygen with minor fractions of other elements.⁴ Various processes including chemical, electrochemical, thermodynamical, and plasma-chemical reactions occur at the discharge sites, due to increased local temperature (10^3 K to 10^4 K) and pressure ($\sim 10^2$ MPa). These processes are responsible for modifying the structure, composition, and morphology of obtained oxide coatings.

2.1. Voltage-time characteristic

Typical voltage versus time characteristic during the anodization of valve metals is shown in Fig. 1.^{5,6} Depending on increasing trend of the voltage, three regions can be clearly identified. From the beginning of anodization the voltage increases linearly with time, resulting in the constant formation rate of thin, compact barrier oxide layer on the substrate. This oxide layer is produced at both metal/oxide and oxide/electrolyte interfaces as a result of migration of O^{2-}/OH^- anions and metal cations Me^{n+} ($n = 2,3,4$ or 5) across the oxide, assisted by a high electric field ($\sim 10^7$ V/cm).⁷ Also, small amounts of anionic components of electrolyte are incorporated into the oxide at the oxide/electrolyte interface during the anodization. Barrier oxide layer is amorphous, it has ionic conductivity and high electrical resistance. Thickness of barrier oxide layer is limited to several hundred nanometers due to the dielectric breakdown under high electric field. This stage of anodization is followed by an apparent deflection from linearity in voltage–time curve, starting from so-called breakdown voltage (stage II). After the breakdown, voltage continually increases, but the voltage–time slope decreases and a large number of small–size microdischarges appear, evenly distributed over the whole sample surface. Further anodization results in relatively stable value of the voltage (stage III).

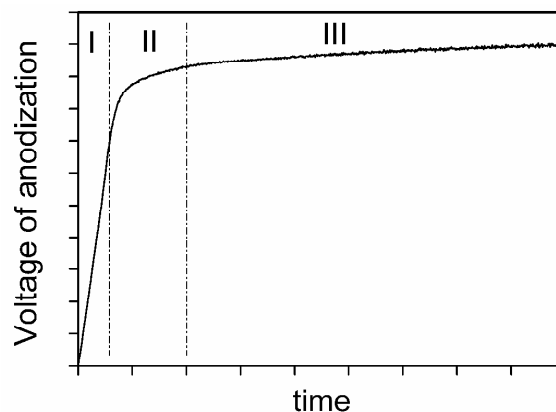


Figure 1. Typical voltage-time dependence during anodization of valve metals.

In the anodization process the total current density is the sum of ionic current density and electron current density.⁸ In the stage I, the electric field strength, for a given current density, remains constant during the anodic growth and the ionic current is two to three orders of magnitude larger than the electronic component. In order to maintain the constant electric field strength, the voltage of anodization increases linearly with time. During anodization electrons are injected into the conduction band of the anodic oxide and accelerated by the electric field, producing avalanches by an impact ionization mechanism.⁸ When the avalanche electronic current reaches its critical value, the breakdown occurs.⁹ In the stage II a relatively low voltage increase (compared with the stage I) is required to maintain the same total current density, due to the independence of the electron current density of the anodic oxide film thickness. In the stage III, the fraction of electron current density in total current density becomes dominant. In this stage, the total current density is almost independent of the anodic oxide film thickness and the voltage-time slope is close to zero.

2.2. Mechanisms of formation of PEO coatings

PEO of valve metals is a complex process combining coexisting partial processes of oxide formation, dissolution, and dielectric breakdown. The main chemical reactions at the metal/oxide interface are:^{2,4,10,11}



where $n = 2,3,4$ or 5 ,



Also, direct ejection of metal into the electrolyte can occur through microdischarge channels during the breakdown:⁴



The main reactions at oxide/electrolyte interface are the formation of gaseous oxygen:



oxidation of the ejected metal:



and chemical dissolution of metal oxides caused by instability of oxide films:



Three main steps lead to formation of oxide coatings during PEO.¹² In the first step, a number of separated discharge channels are formed in the oxide layer as a result of loss in its dielectric stability in a region of low conductivity. This region is heated by generated electron avalanches up to temperatures of 10^4 K.¹³ Due to the strong electric field, the anionic components of electrolyte are drawn into the channels. Concurrently, the metal is melted out of the substrate, enters the channels, and becomes oxidized. As a result of these processes, plasma chemical reactions take place in the channels. These reactions lead to an increase in pressure inside the channels. At the same time, separation of oppositely charged ions occurs in the channel due to the presence of the electric field. The cations are ejected from the channels into the electrolyte by electrostatic forces. In the next step, oxidized metal is ejected from the channels into the coating surface in contact with the electrolyte and in that way the coating thickness around the channels increases. Finally, discharge channels get cooled and the reaction products are deposited on its walls. This process repeats itself at a number of discrete locations over the coating surface, leading to increase in the coating thickness. The

coating material, formed at the sites of breakdown, contains crystalline and amorphous phases, with constituent species derived both from the metal and from the electrolyte.

2.3. Optical emission spectroscopy of microdischarges

The investigation and characterization of microdischarges are important steps in understanding the PEO process. Distribution and types of microdischarges have important effects on the formation mechanism, composition, morphology, and various properties of the resultant oxide coatings. Real-time imaging of the PEO process gives information of the microdischarge spatial density, surface fraction under microdischarges, and the dimensional distribution of microdischarges at various stages of PEO.^{11,14-17}

Given the liquid environment, optical emission spectroscopy (OES) is the best available technique for microdischarges characterization. The most popular application of OES for PEO diagnostics is spectral characterization and observation of temporal evolution of spectral lines in the visible and near UV spectral region. The main difficulty in an application of OES for PEO characterization comes from space and time inhomogeneity of microdischarges appearing randomly across the anode surface. Thus, the PEO spectra represent time integrated radiation recorded by spectrometer-detector system. The results of spectroscopic observation are even more complex to analyze if one takes into account that the radiation intensity is rather low and long exposure times are required. For this reason, high-light power spectrometers with low spectral resolution are usually employed for spectra recordings. Consequently, fine details of spectral line shape of hydrogen lines and narrow line-widths of nonhydrogenic lines are not widely used for PEO characterization.

It has been found that discharge optical emission spectra originate in general from both the species present in substrate and in electrolyte. When the substrate consists of elements with relatively low melting points (Al, Mg), the corresponding atomic and ionic lines appear independently of the type of electrolyte.¹⁸⁻²³ On the other hand, the (non/) appearance of spectral lines of metals with high melting points (Ta, Ti, Zr) strongly depends on the electrolyte.^{16,24-27}

Hydrogen Balmer lines H_{α} (656.28 nm) and H_{β} (486.13 nm) can always be detected during the PEO process, and plasma broadened profiles of these lines were used for electron

number density (N_e) measurement.^{16,17,21,22,24,25,28} Jovović et al. showed that the Balmer line H_α is very intense and strongly self-absorbed in the PEO process.^{17,21,22} For this reason H_α is not suitable for the spectral line shape analysis. Analysis of the Balmer line H_β line profile during PEO of valve metals showed that the H_β line shape can be properly fitted only if two Lorentzian profiles are used.^{16,17,21,22,24,25} These Lorentzian profiles correspond to electron number densities of $N_e \approx 1.0 \times 10^{15} \text{ cm}^{-3}$ and $N_e \approx 2.2 \times 10^{16} \text{ cm}^{-3}$. Spectral line shape analysis of single charge ionic lines of aluminum at 704.2 nm^{21,22} and magnesium at 448.12 nm²¹ were used for electron number density measurement in systems under consideration, and the larger electron number densities $N_e \approx (1.2-1.6) \times 10^{17} \text{ cm}^{-3}$ were obtained.

According to Hussein et al.²⁸ three plasma discharge models have been proposed (see, Fig. 9 in Ref. 28): discharging that occurs at metal/oxide interface (B) and discharging that occurs at oxide/electrolyte interface at either coating upper layer (A) or at the coating top layer (C). The highest N_e measured from single charge ion lines of aluminum and magnesium is emitted from metal plasma generated in the process of type B. Low and medium N_e are related to the processes of type A (discharge in relatively small holes near the surface of oxide layer) and of type C (discharge in the micropores at the surface of oxide layer). Microdischarges that result in evaporation of anodic material (type B) always occur during PEO of aluminum and magnesium (metals with lower melting point) regardless of the type of electrolyte. During PEO of titanium, zirconium, and tantalum (metals with high melting point) occurrence of this type of microdischarges strongly depends on the type of electrolyte.

For plasma electron temperature (T_e) measurement during PEO, relative line intensities were used. This temperature is assumed equal to the electron excitation temperature, calculated from relative line intensities. The application of this approach is based on the assumption of Partial Local Thermal Equilibrium (PLTE) conditions. The discussion of the fulfillment of PLTE is given in ref 21. For plasma electron temperature (T_e) measurement during PEO of aluminum some research groups used the intensity ratio of two Al I lines at 396.2 nm and at 309.1 nm. Upon performed calculations, T_e in the range of (4500–10000) K was determined.²⁸⁻³⁰ Alongside, the intensity ratio of the H_β and the H_α lines was used also for T_e measurements and $T_e = 3480 \text{ K}$ was determined.³¹ We suspect that these results are questionable. First, the Balmer line H_α is self-absorbed, while the H_β interferes with an AlO band.²⁴ Secondly, on the red side of the Al I line at 309.2 nm there is another weaker line

from the same multiplet overlapping with the stronger one. In addition, these lines are Stark and Doppler broadened and positioned within the OH band, which obstructs any line shape analysis. Having this in mind, Jovović et al. used O II lines, which are always present during PEO, to determine T_e .²¹ These lines are sometimes weak but this is an advantage from the point of view of self-absorption. Relative line intensities were used for T_e measurements and upon application of Boltzmann Plot technique $T_e \approx 40000$ K was determined for aluminum.^{21,22} Using the same procedure, electron temperature obtained from Mg I lines is ~ 4000 K,²² from Zr I lines is in the range (7500 ± 1000) K,²⁷ and from Ti I lines in the range (3700 ± 500) K.²⁵

In contrast to the extensive use of atomic emission spectroscopy for investigation of PEO processes and determinations of plasma parameters, there has been very little information about the appearance of molecular bands in the considered systems. Early attempts on this field^{32–34} were restricted to identification of band heads and their more or less provisory assignment. Posuvailo and Klapkiv³² detected the $v' = 0; v'' = 0, v' = 0; v'' = 1$, and $v' = 1; v'' = 0$ bands of the $B \ ^2\Sigma^+ \rightarrow X \ ^2\Sigma^+$ spectral system of AlO. In our previous study on Al,³⁴ we assigned several bands of AlH, AlO, Al₂, and possibly AlH₂. Posuvailo³³ claimed to identify several band heads of β and γ spectral systems of ZrO. However, as shown in our recent study on PEO of Zr,²⁷ the corresponding emission spectrum, and particularly the structure of the ZrO bands are very complex and require much more careful investigation in order to make reliable assignment of the observed features.

3. EXPERIMENTAL

Rectangular samples of dimensions 25 mm \times 10 mm of aluminum (99.999% purity, Goodfellow) and magnesium alloy AZ31 (96% Mg, 3% Al, 1% Zn, Alfa Aesar) were used as working electrodes in experiments. The working electrodes were sealed with insulation resin leaving only active surface area of 1.5 cm². Before the anodization, the surface of the samples was degreased and dried in a warm air stream. The PEO process took place in an electrolytic cell with flat quartz glass windows.³⁵ Two platinum wires (5 cm long and 1 mm in diameter) were used as cathodes. During the PEO, the electrolyte circulated through the chamber–reservoir system and the temperature of the electrolyte was maintained at (20 ± 1) °C.

Aluminum was anodized in 0.1 M citric acid, while magnesium alloy was anodized in 4 g/L $\text{Na}_2\text{SiO}_3 \cdot 5\text{H}_2\text{O}$ and 4 g/L KOH. The electrolytes were prepared by using double distilled and deionized water and PA (pro analysis) grade chemical compounds. Anodizing was carried out at current density of 100 mA/cm^2 .

Spectroscopic measurements were performed utilizing two different grating spectrometers. Spectral measurements during PEO of valve metals in a wavelength range from 380 nm to 850 nm were taken on a spectrometer system based on the intensified charge coupled device (ICCD). Optical detection system consisted of a large-aperture achromatic lens, a 0.3 m Hilger spectrometer (diffraction grating 1200 grooves/mm and inverse linear dispersion of 2.7 nm/mm), and a very sensitive PI-MAX ICCD thermoelectrically cooled camera ($-40 \text{ }^\circ\text{C}$) with high quantum efficiency manufactured by Princeton Instruments.³⁶ The CCD chip consisted of 430×256 active pixels, each approximately $26 \mu\text{m} \times 26 \mu\text{m}$. The system was used with several grating positions with overlapping wavelength range of 5 nm. Spectra were recorded in segments of 43 nm and the whole spectral range was obtained by adding one spectra interval to the previous one. The optical-detection system was calibrated using a LED based light source.³⁷

Spectral measurements during PEO of valve metals in UV region were taken on a spectrometer system consisting of a quartz objective, Czerny-Turner spectrometer, and thermoelectrically cooled ($-10 \text{ }^\circ\text{C}$) CCD detector (2048×506 pixels, each approximately $12 \mu\text{m} \times 12 \mu\text{m}$) manufactured by Hamamatsu. The optical-detection system was calibrated using a hydrogen (D_2) lamp. In both systems, the image of anode surface was projected with unity magnification to the entrance slit of the spectrometers.

4. SPECTROSCOPY OF DIATOMIC MOLECULES

4.1. Hamiltonian of a diatomic molecule

No matter how strange it might sound, the derivation of the complete Hamiltonian for a diatomic molecule is in a certain sense conceptually more demanding than that for a polyatomic molecule with non-linear equilibrium geometry. This is a consequence of the fact that one of the principal moments of inertia (that coinciding with the molecular axis) of a diatomic molecule is

vanishing, what causes anomalous commutation relations between the components of angular momenta and leads to a peculiar form of the rotation part of the Hamiltonian.

Let us consider a molecule with the nuclei A and B whose masses are m_A and m_B , and charge numbers Z^A and Z^B , respectively, and with N electrons (mass = m_e). The total mass of the nuclei (M_n) and of the molecule (M) are thus $M_n \equiv m_A + m_B$, $M = M_n + Nm_e$, respectively. We start with the non-relativistic molecular Hamiltonian defined in a space-fixed coordinate system (SFS). To separate off the translational motion of the molecule, we use an intermediate frame with the axes parallel to those of the SFS and with the origin laying in the mass center of the molecule (involving also the electrons). However, we refer the electron coordinates to the mass center of the nuclei, and we call this frame nuclear center of mass system ($NCMS$). As the three linearly independent nuclear coordinates we chose the components X, Y, Z of the position vector, \vec{r} , of the nucleus B with respect to that of the nucleus A , $\vec{r} = \vec{R}_B - \vec{R}_A$. We define the components of the angular momentum operator of the nuclei, \hat{R} , spatial electron angular momentum, \hat{L} , electron spin operator, \hat{S} , total molecular angular momentum excluding spin, \hat{N} , and total (rovibronic) angular momentum, \hat{J} (we ignore possible presence of the nuclear spins). They satisfy the normal commutation relations,

$$[\hat{M}_x, \hat{M}_y] = i\hbar\hat{M}_z, \quad [\hat{M}_y, \hat{M}_z] = i\hbar\hat{M}_x, \quad [\hat{M}_z, \hat{M}_x] = i\hbar\hat{M}_y, \quad (7)$$

where \hat{M} is \hat{R} , \hat{L} , \hat{S} , \hat{N} , or \hat{J} . Further, all the components of different angular momenta (\hat{R} , \hat{L} , and \hat{S}) commute with one another because they act on different coordinates.

We introduce finally a molecule-fixed coordinate system (MFS) with the goal to separate, as completely as possible, the vibrational from rotational degrees of freedoms. We need the real (original) SFS no more and we rename $NCMS$ into SFS . We choose the MFS so that its z -axis lays along the molecular axis (the direction from the nucleus A towards B) – in this way the rotation of the nuclear skeleton is reduced to the rotation of the MFS . The orientation of this axis with respect to the $NCMS$ is defined by the Euler angles ϕ and θ , which represent thus the rotational coordinates. We fix the value of the third Euler angle χ (that determines the orientation of the x and y axes) to $\chi = 0$. The instantaneous distance between the nuclei, r , is the coordinate whose change corresponds to the vibrations of the nuclei. We denote the spatial

coordinates of the electrons in the *MFS* by x_μ, y_μ, z_μ . The Hamiltonian of the molecule transforms into³⁸

$$\hat{H} = \hat{T}_e + \hat{T}_n + \hat{V}_{en} + \hat{V}_{ee} + \hat{V}_{nn}. \quad (8)$$

\hat{T}_e is the electronic kinetic energy operator:

$$\hat{T}_e = -\frac{\hbar^2}{2m_e} \sum_{\mu=1}^N \left(\frac{\partial^2}{\partial x_\mu^2} + \frac{\partial^2}{\partial y_\mu^2} + \frac{\partial^2}{\partial z_\mu^2} \right) - \frac{\hbar^2}{2M_n} \sum_{\mu=1}^N \sum_{\nu=1}^N \left(\frac{\partial^2}{\partial x_\mu \partial x_\nu} + \frac{\partial^2}{\partial y_\mu \partial y_\nu} + \frac{\partial^2}{\partial z_\mu \partial z_\nu} \right) \quad (9)$$

The nuclear kinetic energy operator has the form

$$\hat{T}_n = \hat{T}_{vib} + \hat{T}_{rot} \quad (10)$$

where

$$\hat{T}_{vib} = -\frac{\hbar}{2\mu} \left(\frac{\partial}{\partial r^2} + \frac{2}{r} \frac{\partial}{\partial r} \right) \quad (11)$$

and

$$\hat{T}_{rot} = \frac{1}{2\mu r^2} \left[(\hat{J}_x - \hat{L}_x - \hat{S}_x)^2 + \frac{1}{\sin \theta} (\hat{J}_y - \hat{L}_y - \hat{S}_y) \sin \theta (\hat{J}_y - \hat{L}_y - \hat{S}_y) \right]. \quad (12)$$

$\mu \equiv m_A m_B (m_A + m_B)$ is the reduced mass of the nuclei. The expressions (11/12) correspond to the volume element $dV_n = r^2 \sin \theta \cdot dr d\theta d\phi$. The potential energy part of the Hamiltonian (8) is

$$\hat{V} = \hat{V}_{en} + \hat{V}_{ee} + \hat{V}_{nn} = \frac{1}{4\pi\epsilon_0} \left\{ -\sum_{\mu=1}^n \left(\frac{Z^A e^2}{R_{A\mu}} + \frac{Z^B e^2}{R_{B\mu}} \right) + \sum_{\mu=1}^N \sum_{\nu>1}^N \frac{e^2}{R_{\mu\nu}} + \frac{Z^A Z^B e^2}{r} \right\}, \quad (13)$$

where $R_{A\mu} = |\vec{R}_\mu - \vec{R}_A| = |\vec{R}_\mu + m_B \vec{R} / M_n|$, $R_{B\mu} = |\vec{R}_\mu - \vec{R}_B| = |\vec{R}_\mu - m_A \vec{R} / M_n|$, $R_{\mu\nu} = |\vec{R}_\nu - \vec{R}_\mu|$.

The components of the electronic spatial and spin angular momenta along the *MFS*-axes are defined in usual way. However, the components of the (rovibronic) angular momentum are³⁸

$$\begin{aligned} \hat{J}_x (= \hat{R}_x + \hat{L}_x + \hat{S}_x) &= i\hbar \frac{1}{\sin \theta} \frac{\partial}{\partial \phi} + \cot \theta (\hat{L}_z + \hat{S}_z), \\ \hat{J}_y (= \hat{R}_y + \hat{L}_y + \hat{S}_y) &= -i\hbar \frac{\partial}{\partial \theta}, \\ \hat{J}_z (= \hat{R}_z + \hat{L}_z + \hat{S}_z) &= (\hat{L}_z + \hat{S}_z). \end{aligned} \quad (14)$$

The components of the electronic angular momenta along the *MFS*-axes have normal commutation relations, analogous to (7). On the other hand, the components of the rovibronic

angular momentum \hat{J} along the *MFS*-axes fulfill the following anomalous commutation relations.³⁸

$$[\hat{J}_x, \hat{J}_y] = -i\hbar \cdot \cot \theta \cdot \hat{J}_x - i\hbar \cdot (\hat{L}_z + \hat{S}_z), \quad [\hat{J}_y, \hat{J}_z] = 0, \quad [\hat{J}_z, \hat{J}_x] = 0. \quad (15)$$

Writing Eqs. (9–12) we separated the kinetic energy operator into three parts, the first (\hat{T}_e) being the electronic kinetic energy operator, the second (\hat{T}_{vib}) involving derivatives with respect to the coordinate r , and the third one (\hat{T}_{rot}) that contains the angular momenta. Note, however, that the separation of the electronic, vibrational, and rotational degrees of freedom is not complete: In the rotation part we also have the vibrational coordinate r as well as the electronic coordinates via the operators \hat{L}_α and \hat{S}_α . The Schrödinger equation corresponding to the kinetic energy operator (9–12) and the potential energy (13) is solved successively. In the framework of the Born–Oppenheimer approximation,³⁹ the electronic part of the Hamiltonian, which involves the electronic kinetic energy operator (9), and the potential energy operator (13), is replaced by the corresponding eigenvalue, $V(r)$, being a function of the coordinate r . In the lowest-order (harmonic) approximation,

$$V(R) = \frac{1}{2} \left(\frac{\partial^2 V}{\partial r^2} \right)_{r=r_e} (r - r_e)^2 \equiv \frac{1}{2} k (r - r_e)^2, \quad (16)$$

where r_e represents the equilibrium value of r . If we replace the volume element dV_n by the more convenient one in the present context, $dV'_n = \sin \theta \cdot dr d\theta d\phi$, Eq. (11) transforms into

$$\hat{T}'_{vib} = -\frac{\hbar}{2\mu} \frac{\partial}{\partial r^2}. \quad (17)$$

The vibration-rotation problem with the Hamiltonian involving the nuclear kinetic energy operator (10) and $V(r)$, playing the role of the potential, can be handled simultaneously for both vibrations and rotations. An alternative way is first to solve the vibrational part of the Schrödinger equation [$\hat{H}_{vib} = \hat{T}_{vib} + V(r)$] and after that the rotational part ($\hat{H}_{rot} = \hat{T}_{rot}$), where the quantity $1/r^2$ in Eq. (12) is replaced by its electronically and vibrationally averaged counterpart $\langle 1/r^2 \rangle$ (in the lowest-order, “rigid-rotor” approximation, $\langle 1/r^2 \rangle = 1/r_e^2$).

4.2. Isomorphic Hamiltonian

A linear molecule only has two rotational degrees of freedom described by the Euler angles ϕ and θ , being sufficient to define the orientation of the internuclear axis (z) in space. At the same time, the third Euler angle χ is arbitrary. The Hamiltonian (8–13) corresponds to the choice $\chi = 0$, but in a more general treatment χ is considered as a certain function of ϕ and θ .^{40,41} The lack of the third Euler angles causes anomalies as unusual commutation relations, Eq. (15), and a strange form of the rotational Hamiltonian, Eq. (12). These problems can be solved introducing the „isomorphic Hamiltonian“.^{42,38,40,41} It has three rotational degrees of freedom (as that of a nonlinear molecule) so that the components of all angular momenta satisfy usual (or „almost“ usual, i.e. up to the sign) commutation relations. On the other hand, the isomorphic Hamiltonian has a number of eigenvalues not being the eigenvalues of the real Hamiltonian. These artificial eigenvalues can, however, be easily eliminated when the Hamiltonian is represented in a suitable basis.

In order to derive the isomorphic Hamiltonian, we introduce χ as an independent variable that defines a new coordinate frame ($x' y' z'$) tied to the molecule; it is obtained from the frame (xyz), corresponding to the choice $\chi = 0$, by rotation through χ about the z -axis. The components of the total angular momentum along the ($x' y' z'$)-axes are^{38,41,43}

$$\begin{aligned}\hat{J}'_x &= -i\hbar \left(-\frac{\cos \chi}{\sin \theta} \frac{\partial}{\partial \phi} + \sin \chi \frac{\partial}{\partial \theta} + \cot \theta \cos \chi \frac{\partial}{\partial \chi} \right), \\ \hat{J}'_y &= -i\hbar \left(\frac{\sin \chi}{\sin \theta} \frac{\partial}{\partial \phi} + \cos \chi \frac{\partial}{\partial \theta} - \cot \theta \sin \chi \frac{\partial}{\partial \chi} \right) \\ J'_z &= -i\hbar \frac{\partial}{\partial \chi}.\end{aligned}\tag{18}$$

They commute with the components of the angular momentum along the SFS -axes, \hat{J}'_x, \hat{J}'_y , and \hat{J}'_z . The operators \hat{J}'_x, \hat{J}'_y , and \hat{J}'_z commute with the components of \hat{L}' and \hat{S}' (along the axes of the same frame), because they act onto different coordinates. However, the commutation relations between \hat{J}'_x, \hat{J}'_y , and \hat{J}'_z are^{41,43–46}

$$[\hat{J}'_x, \hat{J}'_y] = -i\hbar \hat{J}'_z, \quad [\hat{J}'_y, \hat{J}'_z] = -i\hbar \hat{J}'_x, \quad [\hat{J}'_z, \hat{J}'_x] = -i\hbar \hat{J}'_y.\tag{19}$$

They are anomalous [indeed not so extremely anomalous as (15)], because they differ from the normal commutation relations for angular momenta, like those in Eq. (7), in the sign. On the other hand, the electronic angular spatial and spin momenta have normal commutation relations. The anomalous commutation relations of the type (19) have the components along the $x'y'z'$ -axes of all angular momenta which involve nuclear coordinates, like \hat{R} and \hat{N} . Note that the components of the nuclear angular momentum along the MFS -axes in general do not commute with the components of the electronic angular momentum.

The components of the angular momenta along the $(x'y'z')$ -axes are related to the components of \hat{J} along the (xyz) axes, by

$$\begin{aligned}\hat{J}_x - \hat{L}_x - \hat{S}_x &= \cos \chi (\hat{J}'_x - \hat{L}'_x - \hat{S}'_x) - \sin \chi (\hat{J}'_y - \hat{L}'_y - \hat{S}'_y), \\ \hat{J}_y - \hat{L}_y - \hat{S}_y &= \sin \chi (\hat{J}'_x - \hat{L}'_x - \hat{S}'_x) + \cos \chi (\hat{J}'_y - \hat{L}'_y - \hat{S}'_y), \\ \hat{J}_z - \hat{L}_z - \hat{S}_z &= \hat{J}'_z - \hat{L}'_z - \hat{S}'_z = 0.\end{aligned}\quad (20)$$

The rotational Hamiltonian (in cm^{-1}) has in terms of new components of the angular momenta the form

$$\hat{H}_{rot} = \frac{B}{\hbar^2} \left[(\hat{J}'_x - \hat{L}'_x - \hat{S}'_x)^2 + (\hat{J}'_y - \hat{L}'_y - \hat{S}'_y)^2 \right], \quad (21)$$

where $B = \langle \hbar / (4\pi c \mu r^2) \rangle_v$ is the (electronically and) vibrationally averaged rotational constant.

The isomorphic Hamiltonian is defined, taking into account the third relation in Eq. (20) as

$$\hat{H}_{rot}^{iso} \equiv \frac{B}{\hbar^2} \left[(\hat{J}'_x - \hat{L}'_x - \hat{S}'_x)^2 + (\hat{J}'_y - \hat{L}'_y - \hat{S}'_y)^2 + (\hat{J}'_z - \hat{L}'_z - \hat{S}'_z)^2 \right]. \quad (22)$$

Note that the Hamiltonians (12) and (22) are mutually isomorphic but not identical. The border between the identity and isomorphism is crossed by skipping from Eq. (21) to (22), i.e. by using the condition $\hat{J}'_z - \hat{L}'_z - \hat{S}'_z = 0$. Since \hat{H}_{rot}^{iso} commutes with the operator $(\hat{J}'_z - \hat{L}'_z - \hat{S}'_z)$, these two operators have common eigenfunctions, and the mentioned condition will be fulfilled only when we use the basis functions which correspond to the zero eigenvalues of the operator $(\hat{J}'_z - \hat{L}'_z - \hat{S}'_z)$ – only these eigenfunctions of the isomorphic Hamiltonian will be the true wave functions of the operator (12). They are obtained as solutions of the eigenvalue problems

$$\hat{J}'_z \psi_r = \Omega \hbar \psi_r, \quad \hat{L}'_z \psi_e = \Lambda \hbar \psi_e, \quad \hat{S}'_z \psi_s = \Sigma \hbar \psi_s. \quad (23)$$

where Λ and Σ are projections of the operators \hat{L} and \hat{S} on the z' -axis, and $\Omega = \Lambda + \Sigma$.

We shall use further the isomorphic rotation Hamiltonian. To simplify the notation we shall delete the primes and the superscript *iso*. The operator (22) can be written in several alternative forms, depending on whether the relation $\hat{J}_z - \hat{L}_z - \hat{S}_z = 0$ is taken into account explicitly or implicitly. E.g.

$$\hat{H}_{rot} = \frac{B}{\hbar^2} \left\{ \hat{J}^2 - 2\hat{J}_z\hat{S}_z + \hat{S}^2 - \hat{L}_z^2 \right\} - (\hat{J}_+\hat{S}_- + \hat{J}_-\hat{S}_+) - \left[(\hat{J}_+ - \hat{S}_+)\hat{L}_- + (\hat{J}_- - \hat{S}_-)\hat{L}_+ \right] + \frac{1}{2}(\hat{L}_+\hat{L}_- + \hat{L}_-\hat{L}_+); \quad (24)$$

The last term on the right-hand side of Eq. (24), producing no dependence on J , shifts all rotational levels by the same amount and thus we shall consider it as a part of the electronic Hamiltonian (i.e. we neglect it when we only consider rotational structure). The terms involving the products of electronic ladder operators, $\hat{L}_+ \equiv \hat{L}_x + i\hat{L}_y$, $\hat{L}_- \equiv \hat{L}_x - i\hat{L}_y$, and $\hat{J}_\pm / \hat{S}_\pm$ only have off-diagonal electronic matrix elements (i.e. they couple different electronic state). When we calculate the rotational levels in a particular electronic state, the contribution of these terms is small and we shall in general neglect them. (However, they are responsible e.g. for the Λ -splitting in Π states). Such a simplified rotation Hamiltonian can be written as

$$\hat{H}_{rot} = \frac{B}{\hbar^2} \left\{ \hat{J}^2 - 2\hat{J}_z\hat{S}_z + \hat{S}^2 - \hat{L}_z^2 \right\} - (\hat{J}_+\hat{S}_- + \hat{J}_-\hat{S}_+); \quad (25)$$

We shall usually use this form.

The rotational Hamiltonian (24) obviously commutes with \hat{J}^2 , \hat{S}^2 , and \hat{L}^2 , and its approximate form (25) additionally with \hat{L}_z . Recall, however, that the rotational Hamiltonian only represents a part of the total molecular Hamiltonian. The complete molecular Hamiltonian involves besides \hat{H}_{rot} the electronic and vibrational parts, \hat{H}_e and \hat{H}_{vib} , respectively. Since \hat{H}_e does not commute with \hat{L}^2 , the quantum number L , which would correspond to \hat{L}^2 , is never good. Note also that in the rest of the Hamiltonian appear in general the terms that also involve the rotation coordinates, i.e. which take into account the coupling of rotations with the other degrees of freedom. Some of the couplings can be neglected, but there are several of them interfering qualitatively and quantitatively with the rotational structure of molecular spectra. The most important of these is usually the spin-orbit/rotation coupling, because the corresponding effects are on the energy scale comparable

with those caused by molecular rotations. For this reason, we shall below complete the Hamiltonian by the terms describing the leading part of the spin couplings.

In multiplet (i.e. non-singlet) Σ electronic states ($\Lambda = 0$, $S \neq 0$) we have the spin-rotation coupling; we add then to the Hamiltonian (24) or (25) the corresponding operator. We shall represent it in the „phenomenological form“,⁴³

$$\hat{H}_{SR} = \frac{\gamma}{\hbar^2} (\vec{N} \cdot \vec{S}) = \frac{\gamma_v}{\hbar^2} [(\hat{J} - \vec{S}) \cdot \vec{S}], \quad (26)$$

where γ is the (averaged) spin-rotation constant, that may be positive or negative.

In multiplet Π, Δ, \dots ($\Lambda \neq 0$, $S \neq 0$) electronic states the main spin effect is the spin-orbit coupling. It is usually described by the phenomenological operator⁴³

$$\hat{H}_{SO} = \frac{A_{SO}}{\hbar^2} \hat{L} \cdot \hat{S} = \frac{A_{SO}}{\hbar^2} \hat{L}_z \hat{S}_z + \frac{A_{SO}}{2\hbar^2} (\hat{L}_+ \hat{S}_- + \hat{L}_- \hat{S}_+). \quad (27)$$

The matrix elements of the second term on the right-hand side of Eq. (27) are vanishing within an electronic state and do not contribute to the energy in first order. Thus, we usually use the simplified form of the spin-orbit operator,

$$\hat{H}_{SO} \cong \frac{A_{SO}}{\hbar^2} \hat{L}_z \hat{S}_z. \quad (28)$$

A_{SO} is the „spin-orbit constant“, which may, depending on the electron configuration in question, have + or – sign. The spin-rotation coupling is also present in the multiplet spatially degenerate states, but it is there normally much weaker than the spin-orbit one.

In the general case the only operators which commute with the Hamiltonian of a molecule are \hat{J}^2, \hat{S}^2 , and the operator E^* that inverts the coordinates of all particles (electrons and nuclei) in the SFS ; the quantum numbers of these operators are J, S , and + or –, respectively. However, depending on the concrete situation, there may be various near (good) quantum numbers. Such quantum numbers correspond to the operators that do not commute with the complete Hamiltonian, \hat{H} , but they do commute with the dominant part of it, say \hat{H}_1 . The eigenfunctions of \hat{H}_1 build a suitable basis for representation of \hat{H} , and the quantum numbers associated with the operators that commute with \hat{H}_1 label these basis functions. They represent “nearly good” quantum numbers, because the leading part of \hat{H} , namely \hat{H}_1 , is in such a basis represented by a diagonal matrix. The near quantum numbers

are particularly useful for assignment of experimentally observed spectral features. Note that, strictly speaking, even J is not a good quantum number – it is such only in the case of vanishing nuclear spins. In the presence of nuclear spin, \hat{I} , the only good quantum number is that corresponding to the total angular momentum $\hat{F} = \hat{J} + \hat{I}$. However, in this case J is (usually) very nearly a good quantum number.

4.3. Basis functions

The fact that there are three operators \hat{J}^2 , \hat{J}_z , and \hat{J}_z that commute with one another means that there exist sets of their common eigenstates $|J\Omega M\rangle$. Thus,

$$\hat{J}^2|J\Omega M\rangle = J(J+1)\hbar^2|J\Omega M\rangle, \quad \hat{J}_z|J\Omega M\rangle = M\hbar|J\Omega M\rangle, \quad \hat{J}_z|J\Omega M\rangle = \Omega\hbar|J\Omega M\rangle. \quad (29)$$

Non-vanishing matrix elements of the relevant operators in this basis are

$$\begin{aligned} \langle J'\Omega'M'|\hat{J}^2|J\Omega M\rangle &= J(J+1)\hbar^2\delta_{J'J}\delta_{\Omega'\Omega}\delta_{M'M}, \\ \langle J'\Omega'M'|\hat{J}_z|J\Omega M\rangle &= M\hbar\delta_{J'J}\delta_{\Omega'\Omega}\delta_{M'M}, \\ \langle J'\Omega'M'|\hat{J}_\pm^s|J\Omega M\rangle &= \sqrt{J(J+1) - M(M\pm 1)}\hbar\delta_{J'J}\delta_{\Omega'\Omega}\delta_{M',M\pm 1}, \\ \langle J'\Omega'M'|\hat{J}_z|J\Omega M\rangle &= \Omega\hbar\delta_{J'J}\delta_{\Omega'\Omega}\delta_{M'M}, \\ \langle J'\Omega'M'|\hat{J}_\pm^m|J\Omega M\rangle &= \sqrt{J(J+1) - \Omega(\Omega\mp 1)}\hbar\delta_{J'J}\delta_{\Omega',\Omega\mp 1}\delta_{M'M}, \end{aligned} \quad (30)$$

where we introduce the “raising” and “lowering” operators in the *SFS* and *MFS*:

$$\hat{J}_\pm^s \equiv \hat{J}_x \pm i\hat{J}_y, \quad \hat{J}_\pm^m \equiv \hat{J}_x \pm i\hat{J}_y. \quad (31)$$

Note the sign differences in the expressions (30) for matrix elements of these operators. Since we do not deal with external fields, the choice of the quantum number M is arbitrary.

We shall normally use the basis functions corresponding to Hund’s case (a) coupling scheme.^{41,43,46,47} According to it \hat{L} and \hat{S} are both “tied” to the internuclear axis (the z axis of the *MFS*) making the signed projections Λ and Σ , respectively, while \hat{R} is perpendicular to this axis. Thus the total angular momentum \hat{J} makes the projection M on the *SFS* axis Z and the projection $\Omega = \Lambda + \Sigma$ on the *MFS* axis z . Consequently, in this case the rotational basis functions are the symmetric top wave functions $|J\Omega M\rangle$. The total case (a) wave functions are labeled additionally by the electronic spatial quantum numbers n

(“principal” quantum number) and Λ , the spin quantum numbers S, Σ , and the vibrational quantum number ν . We write them in the product form^{41,43}

$$|n, \Lambda^s; \nu; S, \Sigma, J, \Omega, M\rangle = |n\Lambda^s\rangle | \nu \rangle | S\Sigma \rangle | J\Omega(M) \rangle, \quad (32)$$

where s is odd for Σ^- and even for all other electronic states. (The unimportant quantum number M is on the right-hand side put in parentheses.) Actually, the separation $|n\Lambda S\Sigma\rangle = |n\Lambda\rangle |S\Sigma\rangle$ is strictly valid only for one- and two-valence electronic molecules.

Justification for the notation (32) is the following: Each of the operators \hat{L}, \hat{S} , and \hat{J} , appearing in the rotational Hamiltonian only acts on one set of the coordinates and their effect on the vector $|n\Lambda S\Sigma\rangle$ is the same as the effect on the factorized (in the general case, fictitious) form of this vector $|n\Lambda\rangle |S\Sigma\rangle$. The basis (32) is convenient because the key operators $\hat{L}_z, \hat{J}^2, \hat{J}_z, \hat{S}^2$, and \hat{S}_z are all diagonal in this coupling scheme.

Another frequently used basis consists of Hund’s case (b) functions, where the intermediate nearly good quantum number N is used (its projection on the z -axis is Λ) and the spin quantum number Σ is omitted:

$$|n, \Lambda^s; \nu; N, \Lambda, S, J, M\rangle = |n\Lambda^s\rangle | \nu \rangle | SJN\Lambda(M) \rangle. \quad (33)$$

The fact that the components along the *MFS*-axes of some of the momenta we use ($\hat{R}, \hat{N}, \hat{J}$) have anomalous commutation relations, whereas the commutation relations for the other class of operators (\hat{L}, \hat{S}) are normal, causes certain problems. The momenta $\hat{R}, \hat{N}, \hat{J}$, when expressed in terms of their *MFS* components are actually not proper angular momenta, because the angular momentum operator is defined as a vector operator whose components satisfy commutation relations of the type (7). Thus, when working with these operators we cannot directly use a number of relations derived for proper momenta (e.g. those based on the application of the Wigner–Eckart theorem, the Clebsh–Gordan coefficients etc.).⁴⁸ Further, the composite momentum from the standpoint of the theory of addition of angular momenta, \hat{N} [see Eq. (33)], is the difference and not the sum of “partial momenta” \hat{J} and \hat{S} . These problems can generally be solved in three ways. *a*) One can work with the components of all momenta along the *SFS*-axes – all of them satisfy normal commutation relations – and only after carrying out all algebraic manipulation, the results are expressed in terms of the *MFS* components.^{45,46} *b*) The other possibility is to work consequently with the *MFS* components,

bearing in mind anomalies and restrictions mentioned above. *c)* The third way was proposed by Van Vleck:⁴⁴ Instead of momenta $\hat{P}_x, \hat{P}_y, \hat{P}_z$, with anomalous commutation relations like those for $\hat{J}_x, \hat{J}_y, \hat{J}_z$, Eq. (19), we can use the “reverse” momenta

$$\hat{P}_x^r = -\hat{P}_x, \quad \hat{P}_y^r = -\hat{P}_y, \quad \hat{P}_z^r = -\hat{P}_z, \quad (34)$$

which have normal commutation relations,

$$[\hat{P}_x^r, \hat{P}_y^r] = i\hbar\hat{P}_z^r, \quad [\hat{P}_y^r, \hat{P}_z^r] = i\hbar\hat{P}_x^r, \quad [\hat{P}_z^r, \hat{P}_x^r] = i\hbar\hat{P}_y^r. \quad (35)$$

(Indeed, Van Vleck preferred to invert the momenta with normal commutation relations, $\hat{L}_x^r = -\hat{L}_x$, etc. so that all momenta along the *MFS*-axes consistently had anomalous commutation relation.) Consequently, all momenta along the *MFS*-axes ($\hat{L}_x, \hat{S}_x, \hat{R}_x^r, \hat{N}_x, \hat{J}_x, \dots$) have normal commutation relations.

Each wavefunction associated with an energy level may be classified as even or odd according to whether it remains unchanged or changes sign on the operation E^* , carrying out inversion of *SFS* spatial coordinates of all electrons and nuclei. Since the molecular Hamiltonian is invariant under this symmetry operation, it has non-vanishing matrix elements only between the state vectors of the same parity. This operation does not affect the vibrational coordinates. It does not act directly on the spin coordinates, but in the case when the spin angular momenta are quantized along the *MFS*-axes [Hunds’s basis (a)], there is an indirect effect on the spin functions because the transformation from *SFS* to *MFS* involves the Euler angles, being functions of the *SFS* nuclear coordinates. It can be shown that the effect of E^* on Hund’s (a) basis functions is^{41,43}

$$E^* |n\Lambda^s\rangle |v\rangle |S\Sigma\rangle |J\Omega(M)\rangle = (-1)^p |n, -\Lambda\rangle |v\rangle |S, -\Sigma\rangle |J, -\Omega, M\rangle, \quad (36)$$

$p = J - S + s.$

For Hund’s (b) basis,

$$E^* |n\Lambda^s\rangle |v\rangle |N, \Lambda, S, J, M\rangle = (-1)^{N+s} |n, -\Lambda\rangle |v\rangle |N, -\Lambda, S, J, M\rangle \quad (37)$$

It follows that the simple case (a) or case (b) basis functions are not eigenfunctions of E^* . The appropriate combinations which do have a definite parity are in the case (a)⁴¹

$$|n\Lambda^s; JM; \pm\rangle = \frac{1}{\sqrt{2}} \left\{ |n, \Lambda\rangle |v\rangle |S, \Sigma\rangle |J, \Omega, M\rangle \pm (-1)^p |n, -\Lambda\rangle |v\rangle |S, -\Sigma\rangle |J, -\Omega, M\rangle \right\} \quad (38)$$

The $\pm(-1)^{J-S+\sigma}$ phase factor in Eq. (38) causes the parity labels to alternate as J increases, so that the lower of the near-degenerate pair for a given J might be + and the upper –, the designation becomes opposite for the next J value and so on. To avoid this alternation, another parity labeling convention, *ef*, has been introduced.⁴⁹ For integral J , *e*-levels have parity $(-1)^J$ and *f*-levels $(-1)^{J+1}$; for half-integral J , *e*-levels have parity $(-1)^{J-1/2}$ and *f*-levels $(-1)^{J+1/2}$. Following this convention, all lower components of parity doublets have the same label, e.g. *e*, and all the upper components have the opposite label, in this case *f*.

4.4. Transitions

4.4.1. Transition moments

We consider the transition between two states of a diatomic molecule, whose quantum numbers are denoted by prime (upper state) and two prime marks (lower state).^{50,51} We label the corresponding state vectors in the sense of Hund's (a) case. The intensity of the transition between these states is proportional to the square of the transition moment defined as

$$R^{'''} = \left\langle n' \Lambda'; \nu'; S' \Sigma'; J' \Omega' M' \left| \hat{A} \right| n'' \Lambda''; \nu''; S'' \Sigma''; J'' \Omega'' M'' \right\rangle \quad (39)$$

where \hat{A} is the operator which determines the mechanism of the transition. In the case of „optical“ transitions, we consider here, \hat{A} is the (vector) dipole operator, $\hat{\mu}$, defined by

$$\hat{\mu} = \sum_i q_i \vec{r}_i \quad (40)$$

where q_i is the charge, and \vec{r}_i radius vector of the i th particle and the sum runs over all charged particles (electrons, nuclei). The proportionality factor between the intensity of the transition and $|R^{'''}|^2$ involves, beside natural constants and statistical weights, in the case of absorption the energy difference, ΔE , between the levels in question, and at emission ΔE^4 .

In the framework of usually applied non-relativistic, Born–Oppenheimer, and rigid rotator / infinitesimal vibrator approximations the state vectors are assumed in the form of products of partial state vectors for individual degrees of freedom, like on the right-hand side of Eq. (32). If we are only interested in „allowed“ transitions, the spin variables can be excluded from consideration since in this case transitions are only possible when both states

in question have the same spin function ($S'=S'', \Sigma'=\Sigma''$). We start with the expression for the components of the transition moment, $\hat{\mu}_F$, ($F=X, Y, Z$) along the axes of the *SFS*,

$$R_F^{',''} = \langle J' \Omega' | \langle v' | \langle n' \Lambda' | \hat{\mu}_F | n'' \Lambda'' | v'' \rangle | J'' \Omega'' \rangle, \quad (41)$$

where we factorize the state vector, delete the spin parts and arbitrary quantum $M'=M''=M$. Since the electronic and vibrational variables are naturally defined within the *MFS*, we express now the *SFS* components of the dipole operator in terms of their *MFS* counterparts,

$$\hat{\mu}_F = \sum_g \lambda_{Fg} \hat{\mu}_g, \quad (42)$$

where $g=x, y$, or z , and λ_{Fg} are the elements of the rotation matrix which involve *sine* and *cosine* functions of three Euler angles ϕ , θ , and χ . Since (only) the rotation functions depend on the Euler angles (and only on them), Eq. (41) may be transformed into

$$R_F^{',''} = \sum_g \left\langle \left\langle J' \Omega' | \lambda_{Fg} | J'' \Omega'' \right\rangle \left[\langle v' | \langle n' \Lambda' | \hat{\mu}_g | n'' \Lambda'' \rangle | v'' \rangle \right] \right\rangle. \quad (43)$$

The expression

$$\langle n' \Lambda' | \mu_g | n'' \Lambda'' \rangle \equiv R_g^{e',e''}, \quad (44)$$

is the g -component of the “electric transition moment”. It represents the generalization of the usual dipole moment within a single electronic state (when $n'=n''$ and $\Lambda'=\Lambda''$), and unlike the latter it may have both parallel and perpendicular components with respect to the internuclear axis. This quantity is a function of the bond length, r , (i.e. of the vibrational coordinate), and we represent it by a Taylor expansion

$$R_g^{e',e''} = \left(R_g^{e',e''} \right)_{r=r_e} + \left(\frac{dR_g^{e',e''}}{dr} \right)_{r=r_e} (r - r_e) + \dots \quad (45)$$

where r_e is the equilibrium bond length. Inserting (45) into (43) we obtain

$$R_F^{',''} = \sum_g \left\langle \left\langle J' \Omega' | \lambda_{Fg} | J'' \Omega'' \right\rangle \left[\left(R_g^{e',e''} \right)_{r=r_0} \langle v' | v'' \rangle + \left(\frac{dR_g^{e',e''}}{dr} \right)_{r=r_0} \langle v' | (r - r_0) | v'' \rangle + \dots \right] \right\rangle. \quad (46)$$

4.4.2. Electronic transitions

With help of the formula (46) we can discuss all selection rules for optical transitions in diatomic molecules. However, we are dealing in the present study with electronic transitions

($n' \neq n''$ and/or $\Lambda' \neq \Lambda''$) and consider only this case. In the first, Franck–Condon (F–C), approximation we only retain the first term in square parentheses of Eq. (46),

$$R_{F'}^{v',v''} \cong \sum_g \left\langle \left\langle J' \Omega' \middle| \lambda_{Fg} \middle| J'' \Omega'' \right\rangle \left(R_g^{e',e''} \right)_{r=r_0} \right\rangle \langle v' | v'' \rangle. \quad (47)$$

This expression will be nonvanishing if the electric transition moment does not equal zero. This is the case when the product of the irreducible representations of the electronic wave functions equals the irreducible representation of the x , y , or z -components of the dipole operator. In the case of heteronuclear diatomics, the z -component of this operator belongs to the Σ^+ and x - and y -components building together the basis for a Π irreducible representation of the point group $C_{\infty v}$. This results in the selection rule $\Delta\Lambda = 0, \pm 1$. Additional selection rule is that the transitions $\Sigma^+ \leftrightarrow \Sigma^+$ and $\Sigma^- \leftrightarrow \Sigma^-$ are allowed, while the transitions $\Sigma^+ \leftrightarrow \Sigma^-$ are forbidden. In the case of homonuclear diatomics, the z -component of this operator belongs to the Σ_u^+ and x - and y -components to the Π_u irreducible representation of the point group $D_{\infty v}$. This yields the additional selection rule that the electronic transition is allowed only if one of the combining states has g and the other u symmetry.

4.4.3. Vibrational structure of electronic transitions

The square of the scalar product $\langle v' | v'' \rangle$ in Eq. (47), representing the overlap of the vibrational wave functions of the combining state,

$$(FCF)^{e'v',e''v''} = \langle v' | v'' \rangle^2 = \left[\int \psi_{v'}^* \psi_{v''} d\tau_v \right]^2, \quad (48)$$

is the Franck–Condon factor (FCF). We also define the vibrational transition moment (VTM), the vector quantity with the components along the MFS -axes,

$$(VTM)_g^{e'v',e''v''} \equiv R_g^{e'v',e''v''} = \langle v' | \left\langle n' \Lambda' \middle| \hat{\mu}_g \middle| n'' \Lambda'' \right\rangle | v'' \rangle \rangle = \langle v' | R_g^{e',e''} | v'' \rangle \quad (49)$$

In the F–C approximation, $\left| R_g^{e'v',e''v''} \right|^2 = \left| \left(R_g^{e',e''} \right)_{r=r_e} \right|^2 \cdot (FCF)^{e'v',e''v''}$. The magnitude of $|VTM|^2$ or (sometimes significantly less reliably) FCF determines the intensity distribution within a (rotationally unresolved) band system, which consists of bands, each one arising by rotational transitions between a pair of vibrational levels of two electronic states. The most prominent features in band systems are progressions (characterized in absorption by a fixed vibrational quantum number v'' and variable quantum number v' , and fixed v' and variable v'' in emission) and sequences, $v' - v'' = \text{const}$. If the equilibrium bond lengths and vibrational

frequencies are similar in both electronic states, the most intense bands in an experimentally recorded spectrum correspond to the transitions $v'-v''=0$. A long progression with the maximum at a quite large value of $|v'-v''|$ indicates that the equilibrium bond lengths in the combining electronic states are appreciably different. While the bands in a progression are separated from one another by several hundreds to few thousands cm^{-1} (corresponding to the wave numbers of vibrational fundamentals), the separation of the bands in a sequence is usually between several tens and several hundreds cm^{-1} , reflecting the difference in the values of vibrational frequencies in the two electronic states in question.

The F–C approximation is thus mathematically based on the assumption that the electric transition moment is a constant quantity. This corresponds to physical picture of the “vertical” electronic transitions, i.e. the transitions at unchanged distance between the nuclei. If we go beyond the F–C approximation, we have to take into account the dependence of the electric transition moment on the internuclear distance [the second term in of Eqs. (45/46)]. In a diatomic molecule (where the unique vibrational coordinate, r , is totally-symmetric) this only quantitatively influences the transition probabilities; in polyatomic linear molecules it may make the transitions, forbidden in the F–C approximation, “vibronically” allowed.

Measured electronic-vibration terms (in cm^{-1}) are usually represented by the formula

$$\begin{aligned} \frac{E_{v'v''}}{hc} \equiv \tilde{\nu}^{v'v''} = & T_e + \left(v'+\frac{1}{2}\right)\tilde{\nu}' - \left(v'+\frac{1}{2}\right)^2 (\omega_e x_e)' + \left(v'+\frac{1}{2}\right)^3 (\omega_e y_e)' + \dots \\ & - \left(v''+\frac{1}{2}\right)\tilde{\nu}'' + \left(v''+\frac{1}{2}\right)^2 (\omega_e x_e)'' - \left(v''+\frac{1}{2}\right)^3 (\omega_e y_e)'' + \dots \end{aligned} \quad (50)$$

where T_e is the electronic term value and $\tilde{\nu}$ is the vibrational wave number. T_e is the energy difference between the minima of the potential curves for the upper and lower electronic state; it is actually a quantity that is not directly measured and plays in Eq. (50) just the role of a fitting parameter. Note that Herzberg used instead of $\tilde{\nu}$ the symbol ω_e (as well as ω) and called it “vibrational frequency measured in cm^{-1} ”.⁴⁷ (The subscript “e” in ω_e stands for “equilibrium”.) On the other hand, we retain the notation $(\omega_e x_e)$ and $(\omega_e y_e)$ for the experimentally determined anharmonicity parameters expressed in cm^{-1} and the parentheses should indicate that we shall always handle these products as single quantities.

We have used the experimentally derived formula (50) for assignment of bands observed in our spectra. However, for determination of the plasma temperature we also need the *FCFs* and/or *VTMs*. In order to calculate these quantities we have to solve the vibrational Schrödinger equation for two electron states in question and to use the so obtained wave functions to compute the required quantities. If one wishes to avoid explicit *ab initio* calculations of the potential energy curves for the electronic states in question, he has first to find a way how to extract the potential energy function that, combined with the corresponding kinetic energy operator, gives the energy eigenvalues as close as possible to those presented by the formula (50). We have solved this problem combining the quantum-mechanical perturbative and variational approaches.

We assume the vibrational Hamiltonian in the form

$$H = H^0 + V', \quad (51)$$

where

$$H^0 = -\frac{\hbar^2}{2\mu} \frac{d^2}{dx^2} + \frac{1}{2} kx^2 \quad (52)$$

and

$$V' = k_3 x^3 + k_4 x^4 + \dots; \quad (53)$$

where $x \equiv (r - r_e)$. Applying the perturbation theory we can relate the force constants k , k_3 , k_4 ... to the coefficients in the expansion (50).⁵² We shall use below only the first two of them:

$$k = \mu\omega^2 = 4\mu\pi^2 c^2 \tilde{\nu}^2, \quad (54)$$

and

$$k_3^x = \frac{2}{\sqrt{15}} \frac{\mu^{3/2} \omega^2}{\hbar} \sqrt{(\omega_e x_e) hc}. \quad (55)$$

In variational calculations of the eigenvalues and eigenfunctions of an anharmonic oscillator, as well as of the *FCFs* and *VTMs* for particular combinations of vibrational levels of two electronic state, the following procedure is applied:⁵³ One of the electronic states, a , (typically ground state) is chosen as the referent one. The basis functions (being the eigenfunctions of a suitably chosen harmonic oscillator) are centered with respect to its equilibrium bond length, r_e . If the potential energy curve is *ab initio* computed, it is fitted to

a polynomial of the type (53). The potential energy curve of the other state, b , is fitted by polynomial series in the same variable as for the reference state,

$$V_b = k_0^b + k_1^b(r - r_e) + k_2^b(r - r_e)^2 + k_3^b(r - r_e)^3 + \dots \quad (56)$$

where r_e is (as before) the equilibrium bond length in the ground electronic state. In this case we have also a constant and a linear term in $(r - r_e)$, because the two states in question have different equilibrium bond lengths and their minima are separated in energy. Of course, we may use instead of *ab initio* computed potentials their experimentally derived counterparts. In variational calculations the eigenfunctions for the v 'th level of the electronic state a and the v' 'th level of the state b are obtained in the form

$$|\psi_{v''}\rangle = \sum_i c_i^{v''} |\psi_i^{(0)}\rangle, \quad |\psi_{v'}\rangle = \sum_j d_j^{v'} |\psi_j^{(0)}\rangle, \quad (57)$$

where $|\psi_i^{(0)}\rangle$ are the basis functions, and $c_i^{v''}$ and $d_j^{v'}$ are the expansion coefficients. The advantage of the choice of the same basis for both states becomes now clear. The *FCF* for the two vibrational states in question is simply

$$(FCF)^{e^{v'}, e^{v''}} = \left[\sum_j d_j^{v'} \langle \psi_j^{(0)} | \sum_i c_i^{v''} |\psi_i^{(0)}\rangle \right]^2 = \left[\sum_i d_i^{v'} c_i^{v''} \right]^2. \quad (58)$$

When the bond-length dependence of the electric transition moment is taken into account, it is fitted to the form

$$R^{e', e''} = \sum_k R_k (r - r_e)^k, \quad (59)$$

and the *VTM* is computed as

$$R^{e^{v'}, e^{v''}} = \sum_j d_j^{v'} \langle \psi_j^{(0)} | \sum_k R_k (r - r_e)^k \sum_i c_i^{v''} |\psi_i^{(0)}\rangle = \sum_i \sum_j \sum_k d_j^{v'} c_i^{v''} R_k \langle \psi_j^{(0)} | (r - r_e)^k | \psi_i^{(0)}\rangle. \quad (60)$$

The intensity of the spectral band appearing as a consequence of the emission transition between the vibrational level v' of the electronic state e' and the vibrational level v'' of the electronic e'' is determined by the formula

$$I_{e^{v'}, e^{v''}} \propto N_{v'} (E_{v'e'} - E_{e^{v''}})^4 \left| \bar{R}^{e^{v'}, e^{v''}} \right|^2 e^{-\frac{E_{v'e'} - E_{e^{v''}}}{kT}} \quad (61)$$

Where $E_{v'e'}$ and $E_{e^{v''}}$ are the energies of these two states, $N_{v'}$ is the number of molecules in the upper state, k is the Boltzmann constant, and T the temperature. Since the wave number differences between all bands we used in the present study for determination of temperature,

namely the members of the band sequences $\nu' - \nu'' = 0, -1, -2$, are negligibly small compared to the energy of the electronic transition, the quantity $E_{\nu'e'} - E_{\nu''e''}$ can in Eq. (61) be assumed constant and then the number of the molecules in the upper state is

$$N_{\nu'} \propto \frac{I_{e'\nu',e''\nu''}}{|\bar{R}_{e'\nu',e''\nu''}|^2}. \quad (62)$$

In the F-C approximation, it is assumed that the electric transition moment is constant, and in this case we replace in the formula (62) $|\bar{R}_{e'\nu',e''\nu''}|^2$ by the *FCF*.

Assuming a partial local thermal equilibrium of the system, the ratio of the number of molecules $N_{e'\nu'}$ in the vibrational state ν' and in the lowest vibrational state $\nu' = 0$ of the same electronic species, $N_{e'0}$ is determined by

$$\frac{N_{e'\nu'}}{N_{e'0}} = e^{-\frac{E_{e'\nu'} - E_{e'0}}{kT}}. \quad (63)$$

Combining the formulae (62) and (63), we obtain for the sequence $\nu' - \nu'' = -\Delta\nu$

$$\ln \left(\frac{\frac{I_{e'\nu',e''\nu'+\Delta\nu}}{|\bar{R}_{e'\nu',e''\nu'+\Delta\nu}|^2}}{\frac{I_{e'0,e''\Delta\nu}}{|\bar{R}_{e'0,e''\Delta\nu}|^2}} \right) = - \left(\frac{E_{e'\nu'} - E_{e'0}}{k} \right) \frac{1}{T}, \quad (64)$$

or, in the F-C approximation,

$$\ln \left[\frac{\frac{I_{e'\nu',e''\nu'+\Delta\nu}}{(FCF)^{e'\nu',e''\nu'+\Delta\nu}}}{\frac{I_{e'0,e''\Delta\nu}}{(FCF)^{e'0,e''\Delta\nu}}} \right] = - \left(\frac{E_{e'\nu'} - E_{e'0}}{k} \right) \frac{1}{T}. \quad (65)$$

We use below the formulae (64) and/or (65) to determine the plasma temperature. This approach has the advantage that it does not require the knowledge of the Einstein transition probabilities and that the measured peaks appear in a narrow spectral range such that the problems caused by wavelength dependence of the measurement sensitivity are avoided.

4.4.4. Rotational structure of electronic transitions

The general selection rule for rotational transitions is

$$J' - J'' = 0, \pm 1, \quad (66)$$

with the restriction that the transition $J = 0 \leftrightarrow J = 0$ is forbidden. However, the presence of electronic spatial and spin angular momenta introduced additional, not rigorous selection rules. In transitions involving Hund's (a)-type states (large spin-orbit constant, typical for molecules with relatively heavy nuclei and nonvanishing electronic spatial and spin angular momenta), the projection of the total electron angular momentum (involving both the spatial and spin contributions) on the internuclear axis, $\Omega \equiv \Lambda + \Sigma$ (being at the same time the projection of the total angular momentum) is nearly conserved. In this case we have the additional selection rule $\Delta\Omega = 0$. In the other extreme case of relatively weak spin effects, like in Σ electronic states or in molecules with light atoms, particularly at strong rotation [Hund's case (b)] the $\Delta\Omega = 0$ selection rule is replaced by $\Delta N = 0, \pm 1$ (with the restriction that $\Delta N = 0$ does not occur in $\Sigma-\Sigma$ electronic transitions). A more detailed discussion of the rotational structure of electronic spectra will be given below for each spectral system considered in the present study.

4.5. Sources of experimental data

The classical sources of information about molecular spectra represent the monographs by Herzberg^{47,54-56} and Pearse and Gaydon.⁵⁷ In Herzberg's (*H*) volumes I⁴⁷ and III⁵³ are collected all relevant experimental data up to fifties/sixties of the preceding century. In the fourth volume, published in 1979 in collaboration with Huber (*HH*),⁵⁶ one can find the data on diatomic molecules reported until the end of 1975. The fourth (to our knowledge the last one) edition of the book by Pearse and Gaydon (*PG*) is printed in 1976, i.e. almost at the same time as the *HH*'s compilation of data on diatomics. This edition contains the data published until the end of 1974. Thus, at searching for information about molecular spectra, one has practically only to look at experimental papers published after appearance of the mentioned monographs, and to complete in this way the information collected by *H/HH* and *PG*. These books have become such a standard source of information on molecular spectra, that many authors of new studies do not cite explicitly the authors of old experimental works but they simply quote these studies as "*H* or *PG* and the references therein". We will in general follow this praxis in the present review.

While the three volumes by Herzberg^{47,54,55} involve also complete theory underlying molecular spectra, as well as numerical values for all molecular parameters like vibrational

frequencies and anharmonicity constants, rotational constants, internuclear distances, etc., the book by *PG* only involves the results of direct spectral measurements, i.e. positions of band heads and their relative intensities. Thus, the books by *H* and *PG* are in a sense complementary. It should be noted that in the *H*'s books the transition energies are given in wave numbers for vacuum, whereas they are collected by *PG* in wavelengths, as measured in air. Therefore, a *PG* wavelength is not exactly the inverse of the corresponding *H*'s wave number.

4.6. On the interplay between molecular spectroscopy and quantum chemistry

One of the greatest spectroscopists, D.A. Ramsay, presented at a Conference (Breukelen, Holland) in 1976 an interesting table (Table. 1, first and second column with error margins). It showed what experimentalists expected from the theoreticians at that time (i.e. forty years ago): Not necessarily data of spectroscopic accuracy but rather results with definite error margins that would help answer some important questions, which could not be answered on the basis of experiments alone. So, e.g., the theoretical information about the occurrence and mutual interactions of various electronic states in a certain energy range was very valuable for the experimentalists; the help of theoreticians was sought when it was not possible to assign unambiguously the spectral lines observed. Ramsay gave two sets of error margins, which he named “acceptable” and “good”. It is clear that the error limits quoted in Table 1 as “acceptable” hardly possessed any predictive value – they only could have been of some help in the interpretation of general features of spectra. On the other hand, the situation was different with the “good” theoretical results: In a number of cases it has been shown that results of such accuracy have lead to reliable predictions of spectra not observed before.

About twenty years ago (i.e. in 1995) one of the authors of the present study showed in a review paper⁵¹ another table with the accuracy of *ab initio* results for a number of triatomic molecules involving the atoms from the first three periods of the Periodic table. It is included in Table 1 in the column “state of the art (1995)”. The results were obtained in the eighties and nineties of the preceding century, and concerned the pairs of lowest-lying electronic species correlating with a degenerate (Π or Δ) electronic state at the linear molecular geometry. The calculations of the one-dimensional potential energy curves have been performed employing the atomic orbital basis sets involving s and p functions for hydrogen

atoms, and s, p, and d functions for heavier atoms. Only in some cases f-type basis functions have been used. A typical number of contracted gaussian basis functions employed in these calculations was, say, 50. The final results were obtained by means of quite modest multi-reference (single and) double excitation configuration interaction method (MRDCI) calculations. As seen from Table 1, the overall accuracy was comparable to that qualified by Ramsay as “good”.

Nowadays the *ab initio* calculations are carried out at a much higher level of sophistication, i.e. by employing tremendously more computer and human time (last column in Table 1). In the first of the two *ab initio* studies we will discuss below, published in 1999 (Table 3), only the oxygen atom was described by 80/109, and in the second one from 2010 (Table 7) even with 145 contracted gaussians. At the first glance the accuracy of the results is, except for the vibrational frequencies, the same as before. However, it should be noted that the error margins for the electronic energies quoted in the last column concern great number of electronic states, many of them being highly excited.

Table 1. Expected accuracy of quantum chemical calculations

quantity	acceptable (1976)	good (1976)	state of the art (1995)	state of the art (2014)
$r, \Delta r$	0.05 Å	0.01 Å	0.01 Å	0.01 Å
θ	5 degrees	1 degree	1–2 degree	
$\Delta E, D, I$	0.5 eV	0.1 eV	0.05 eV	0.05 eV
ω	250 cm ⁻¹	50 cm ⁻¹	100–200 ^a , 50 ^b cm ⁻¹	10 ^a cm ⁻¹
μ	0.5 D	0.1 D		
f	250 %	50 %		

r ≡ equilibrium bond length; θ ≡ equilibrium bond angle; ΔE ≡ vertical electronic transition energy; D ≡ dissociation energy; I ≡ ionization potential; ω ≡ vibrational frequency; μ ≡ dipole moment; f ≡ oscillator strength. ^a ≡ stretching frequency; ^b ≡ bending frequency. For further explanation see the text.

The content of Table 1 justifies the strategy we apply at assignment of our spectral results and their use for determination of the plasma parameters, like the temperature and electron number density. In any case when we have at disposal the results of direct high-resolution spectroscopic measurements, like positions of spectral lines/bands, we use them to assign our spectra. The reason for that is not only that these results are more accurate than their *ab initio* counterparts: Even if the theoretical results for e.g. electronic energy differences and vibrational frequencies were exact, it would not be easy to assign with help of them unresolved structure of our molecular bands, where we only can identify the (sub-)band heads. We have similar situation with the rotational constants and equilibrium bond lengths. Although these quantities are not directly measured, their precise values can (in diatomic molecules) be easily determined based on the rotationally resolved spectra. On the other hand, the *ab initio* computed rotational constants are less accurate, because of their quadratic dependence on the equilibrium bond lengths, the latter quantities not yet being computed accurately enough by *ab initio* methods. On the contrary, there are some quantities that are easier to calculate than to measure. Such is, e.g. the electric transition moment, and particularly its dependence on the instantaneous bond length. If we have accurate potential energy curves and equilibrium bond lengths (and these quantities can be extracted from experimental findings) it is then easy, e.g. as described in subsection 4.4.3, to compute accurate intensity distributions.

5. SPECTRUM OF MgO

5.1. Spectral systems of MgO

Selected data for MgO, taken from *HH*,⁵⁶ are presented in Table 2.

Table 2.⁵² A part of the table with molecular constants for $^{24}\text{Mg}^{16}\text{O}$ given by *HH*.⁵⁶

State	T_e (cm^{-1})	ω_e (cm^{-1})	$\omega_e x_e$ (cm^{-1})	r_e (\AA)	Observed transitions	ν_{00} (cm^{-1})
$G^1\Pi$	[40259.8]			[1.834]	$G \rightarrow A$ $G \rightarrow X$	36365.4 39868.6
$F^1\Pi$	(37922)	[696]		[1.772 ₈]	$F \rightarrow X$	37879.1

$E^1\Sigma^+$	(37722)	[705]		[1.829]	$E \rightarrow A$	34180
					$E \rightarrow X$	37683.5
$C^1\Sigma^-$	30080.6	632.4	5.2	[1.872 ₉]	$C \rightarrow A$	26500.94
$e^3\Sigma^-$					$(e \leftarrow a)$	
$D^1\Delta$	29851.6	632.5	5.3	1.871 ₈	$D \rightarrow A$	26272.04
$d^3\Delta_i$	(29300)	(650)		(1.8 ₇)	$(d \leftrightarrow a)$	26867
$c^3\Sigma^+$	(28300)				$(c \leftarrow a)$	25900
$B^1\Sigma^+$	19984.0	824.0 ₈	4.7 ₆	1.737 ₁	$B \rightarrow A$	16500.2 ₉
					$B \leftrightarrow X$	20003.5 ₇
$A^1\Pi$	3563.3	664.4 ₄	3.91	1.864 ₀		
$a^3\Pi_i$	(2400)	(650)		(1.8 ₇)		
$X^1\Sigma^+$	0	785.0 ₆	5.1 ₈	1.749 ₀		

In the book by *PG*⁵⁷ there are data about five spectral systems of MgO, namely of a strong green, a weaker red, and several ultra-violet systems. The red system, consisting of single-headed bands degraded to the violet, appears in the wavelength range 690–470 nm and is assigned to the $B^1\Sigma^+ - A^1\Pi$ electronic transition. The data were taken from references 58–60. The information about the green system, assigned to $B^1\Sigma^+ - X^1\Sigma^+$, was taken from Mahanti⁵⁸ and Lagerqvist.⁶¹ This spectrum appears in standard sources like arc and flames, but also in the sun-spots. The bands are embedded in the wavelength region 521 – 476 nm. The system is dominated by a very marked (0,0) sequence and the bands are degraded to the violet. The data about the violet systems of MgO, appearing between 396 and 364 nm originate from several studies.^{62–66} Two systems of red-degraded bands $C^1\Sigma^- - A^1\Pi$ and $D^1\Sigma^- - A^1\Pi$, and a violet-degraded $^3\Delta - ^3\Pi$ system were detected. Besides, the identification of three other red-degraded ultra-violet systems appearing at 265.2 nm ($E^1\Sigma^+ - X^1\Sigma^+$), 263.7 nm ($F^1\Pi - X^1\Sigma^+$), and 255.6 nm ($G^1\Pi - X^1\Sigma^+$) was reported [22–24].^{67–69} A violet-degraded band, assigned to $G^1\Pi - A^1\Pi$, was detected at 275.01 nm.

Newer experimental studies, including optical spectroscopy, laser-magnet resonance, laser-induced fluorescence, two-color resonance-enhanced two-photon ionization studies, and vibrationally resolved photoelectron spectroscopy^{70–82} have been cited in the comprehensive theoretical study by Maatouk et al.⁸³

5.2. Quantum chemical studies on MgO

The MgO molecule has been subject of several *ab initio* studies.^{75,83–96} We shall rely our discussion on the most exhaustive one, carried out by Maatouk et al.⁸³ These benchmark

electronic structure calculations were performed using the MOLPRO program suite.⁹⁷ The procedure involved complete active self-consistent field (CASSCF)⁹⁸ approach with the cc-pV5Z atomic orbital basis sets,^{99,100} followed by the internally contracted multi-reference configuration interaction (MRCI) method.^{101,102} The potential energy curves, electric transition moments, and spin-orbit matrix elements were computed for a large number of singlet, doublet, and quintet electronic states. Selected results of these calculations are presented in Table 3. They are compared with their experimentally derived counterparts, in order to present to the reader the state of the art of modern *ab initio* computations.

Table 3.⁵² Comparison of the results of *ab initio* electronic structure calculations on MgO⁸³ with the corresponding experimentally derived quantities.

State	T_e (cm ⁻¹)	$(T_e)_{\text{exp}}$ (cm ⁻¹)	ω_e (cm ⁻¹)	$(\omega_e)_{\text{exp}}$ (cm ⁻¹)	$\omega_e x_e$ (cm ⁻¹)	$(\omega_e x_e)_{\text{exp}}$ (cm ⁻¹)	r_e (Å)	$(r_e)_{\text{exp}}$ (Å)
3 ³ Δ	52321		340.8		1.85		2.367	
3 ³ Σ ⁻	51748		337.5		2.03		2.356	
2 ¹ Σ ⁻							∞	
4 ¹ Π	44987.9		891.8		1.31		2.172	
1 ⁵ Π	41390.0		141.2		5.42		2.577	
G ¹ Π	40364.1	40259.8 ^a	621.4		2.59		1.869	1.834 ^a
2 ¹ Δ	39173.6		601.3		85.71		2.650	
E ¹ Σ ⁺	39113.1	37722 ^a 37719 ^b	698.1	705 ^a 714.2 ^b	10.95	4.18 ^b	1.837	1.829 ^a 1.83 ^b
3 ³ Π	38050.9	39967 ^c	880.5		59.25		1.921	
F ¹ Π	37322.6	37922 ^a 37919 ^c	699.2	696 ^a 705 ^c 711 ^d	5.12	4.5 ^c	1.786	1.772 ^a 1.766 ^c 1.77 ^d
2 ³ Σ ⁻	31520.3		798.4		28.95		1.991	
e ³ Σ ⁻	30076	31250 ^a					∞	∞ ^a
C ¹ Σ ⁻	29516.1	30080.6 ^a	626.9	632.4 ^a	4.19	5.2 ^a	1.886	1.873 ^a
D ¹ Δ	29228.2	29851.6 ^a 29835.4 ^c	625.1	632.5 ^a 631.6 ^c	4.27	5.3 ^a 5.2 ^e	1.886	1.8718 ^a 1.8606 ^c
d ³ Δ	28930.5	29300 ^a 29466.2 ^e	653.5	650 ^a 655.2 ^c	4.34	4.9 ^e	1.875	1.87 ^a 1.8710 ^e
2 ³ Π	28218.4		283.4		1.61		2.799	
c ³ Σ ⁺	27703.0	28300 ^a	642.4		4.60		1.880	
B ¹ Σ ⁺	19332.7	19984.0 ^{a,f,j} 19982.6 ^g	808.2	824.08 ^a	3.79	4.76 ^a	1.753	1.737 ^a
b ³ Σ ⁺	7726.6		673.7		4.37		1.807	
A ¹ Π	3078.5	3563.3 ^{a,f}	654.3	664.4 ^a	4.03	3.91 ^a	1.879	1.864 ^a

		3561.9 ^g						
		3563.8377 ^h		664.3929 ^h		3.9293 ^h		1.864325 ^h
		3560.1 ⁱ		664.3 ⁱ		3.8 ⁱ		1.8636 ⁱ
		3563 ^j		664.4765 ^j		3.9264 ^j		
		3558.50124 ^k		664.4360 ^k		3.92853 ^k		
$a^3\Pi$	1645.4	2400 ^a	644.8	650 ^a	5.3		1.885	1.87 ^a
		2492.5 ^c		691.1 ^c		4.0 ^c		
		2623 ^g		648 ^g		3.9 ^g		
				648.3 ^l		3.9 ^l		
		2620.6 ⁱ		650.2 ⁱ		4.2 ⁱ		1.8687 ⁱ
		2618.9453 ^k		650.18028 ^k		4.2 ^k		
$X^1\Sigma^+$	0	0	769.0	785.06 ^{a,f}	4.45	5.18 ^{a,f}	1.766	1.749 ^a
		0		785.2183 ^j		5.1327 ^j		
		0		785.14 ^g		5.07 ^g		
		0		785.262621 ^k		5.12379 ^k		

a: Ref. 56, and references therein; b: Ref. 80; c: Ref. 79; d: Ref. 82; e: Ref. 72; f: Ref 103; g: Ref. 70; h: Ref. 74; i: Ref. 73; j: Ref. 77; k: Ref. 81; l: Ref. 71.

We consider here the results for the $X^1\Sigma^+$ and $B^1\Sigma^+$ electronic states (and the neighboring species), being involved in the electronic transition we shall discuss below.

In the ground electronic state, $X^1\Sigma^+$, and not far from the equilibrium geometry [F–C region], the MgO molecule has two dominating electronic configurations, ... $5\sigma^2 6\sigma^1 2\pi^4 7\sigma^1$ and ... $5\sigma^2 6\sigma^2 2\pi^4$. At large MgO distances, the latter one becomes predominating. In the F–C region, the lowest-lying excited electronic states (embedded only about 0.2–0.4 eV above the ground state) of MgO are $a^3\Pi$ and $A^1\Pi$, both of them corresponding to the ... $5\sigma^2 6\sigma^2 2\pi^3 7\sigma^1$ electronic configuration. All three electronic species are strongly mixed by rotational or spin–orbit couplings. The next two excited states are $b^3\Sigma^+$ and $B^1\Sigma^+$. The $b^3\Sigma^+$ state has ... $5\sigma^2 6\sigma^1 2\pi^4 7\sigma^1$ as the dominant configuration, while the $B^1\Sigma^+$ state, with the vertical energy of about 2.5 eV (corresponding roughly to 20.000 cm^{-1}) is in the F–C region dominated by the same electronic configurations as the ground state. Consequently, the equilibrium bond lengths and vibrational frequencies are similar in the $B^1\Sigma^+$ and $X^1\Sigma^+$ states, but these spectroscopic parameters are quite different from their counterparts in the other electronic species mentioned. Upon enlarging bond length, the $B^1\Sigma^+$ electronic state is continuously more dominated by the electronic configurations ... $5\sigma^2 6\sigma^2 2\pi^4$ and ... $5\sigma^2 6\sigma^2 2\pi^2 6\sigma^2$, and thus at these geometries it differs considerably from the $X^1\Sigma^+$ state. Because of that, the electric transition moment between these two species shows a strong dependence on the bond

length, as seen in Fig. 5 of Ref. 86. The other electronic states of MgO lie in the F–C region at considerably higher energies (> 3.5 eV).

5.3. $B^1\Sigma^+ \rightarrow X^1\Sigma^+$ system of MgO

5.3.1. Rotational structure of the electronic transition

In the simplest case of singlet Σ electronic states ($\Lambda = 0$, $S = 0$), $\hat{J} = \hat{N} = \hat{R}$, and the isomorphic rotation Hamiltonian (24/25) reduces to

$$\hat{H}_{rot} = \frac{B}{\hbar^2} \hat{J}^2 = \frac{B}{\hbar^2} \hat{N}^2 = \frac{B}{\hbar^2} \hat{R}^2 \quad (67)$$

This Hamiltonian is analogous to the angular part of the Hamiltonian for the hydrogen atom. In this case the rotation wave functions, whose general form is $|J\Omega M\rangle$, reduce to $|J0M\rangle$ [the quantum number $\Omega (= K) = \Lambda + \Sigma$ equals in the present case zero], i.e. to spherical harmonics. The eigenvalues (in cm^{-1}) of the Hamiltonian (67) are

$$\tilde{\nu} = BN(N+1) = BJ(J+1). \quad (68)$$

The rotation levels are $2N+1$ degenerate because the wave functions depend on the quantum number M too, taking for a given N all integer values between $-N$ and N . In Σ states the effect of the spatial inversion on the electronic wave functions is the same as that of the reflection in the planes involving the molecular axis, $E^*\Sigma^\pm = \sigma_v\Sigma^\pm = \pm\Sigma^\pm$. The parity of rotational levels is $(-1)^J$, i.e. in $^1\Sigma^+$ states the overall parity of the levels with even J is positive, whereas the levels with odd J have negative parity. Consequently, all the levels of a $^1\Sigma^+$ state are e^- levels.

The selection rule for rotational transitions when both electronic states are of $^1\Sigma$ symmetry is $J' = J'' + 1$ („R branch“) and $J' = J'' - 1$ („P branch“). Let us take $J'' = J$. When the effects of anharmonicity can be neglected, then we have for the R branch $J' = J + 1$, and the term values are

$$\begin{aligned} \tilde{\nu} &= \tilde{\nu}_0 + F'(J') - F''(J'') = \tilde{\nu}_0 + B'(J+1)(J+2) - B''J(J+1) = \\ &= \tilde{\nu}_0 + 2B' + (3B' - B'')J + (B' - B'')J^2, \end{aligned} \quad (69)$$

where $\tilde{\nu}_0$ is a constant for the given electronic-vibrational transition, the „band origin“. For the P branch, $J' = J'' - 1 = J - 1$, and the term values are thus

$$\tilde{\nu} = \tilde{\nu}_0 + F'(J') - F''(J'') = \tilde{\nu}_0 + B'(J-1)J - B''J(J+1) = \tilde{\nu}_0 - (B'+B'')J + (B'-B'')J^2. \quad (70)$$

When $B' > B''$, as in the present case, the contribution of the linear term in J in Eq. (70) is negative, while the contribution of the quadratic term is positive. At small J values the linear term dominates, but the difference in the contribution of the linear and quadratic term becomes continuously smaller with increasing J , at a certain J value, $J = J_h$, they equalize, and after that the quadratic term becomes dominant. Around the $J = J_h$ value (vertex of the parabola) the rotational lines are crowded and build a „band head“. It appears at a wave number lower than that of the band origin, $\tilde{\nu}_0$, i.e. at the „red side“ with respect to $\tilde{\nu}_0$. The band is „shaded“ („degraded“) towards the violet (i.e. towards shorter wave lengths). The position of the band head is found when the condition $d\tilde{\nu}/dJ = 0$ is fulfilled. In the case when $B' > B''$, e.g., differentiating Eq. (70) we obtain

$$J_h = \frac{(B'+B'')}{2(B'-B'')}. \quad (71)$$

Replacing in Eq. (70) J with J_h given by Eq. (71), we obtain for the term difference between the band head and the (real or extrapolated) band origin

$$\tilde{\nu}_h - \tilde{\nu}_0 = -\frac{(B'+B'')^2}{4(B'-B'')}. \quad (72)$$

5.3.2. Identification of bands

In our study on PEO of magnesium,¹⁰⁷ we recorded an optical emission spectrum in the wavelength range from 370 nm to 850 nm. It consisted of a number of atomic and ionic lines that originated either from magnesium alloy electrode or from the electrolyte. Besides, we identified several bands, the most pronounced of them appearing in the spectral range between 500 and 420 nm (19950–24000 cm^{-1}). In this narrower wavelength range we recorded a series of spectra corresponding to different time delays with respect to the beginning of the PEO process. A typical spectrum is displayed in Fig. 2. It appears as a broad peak with clearly pronounced structure. The most intense sub-peak is at 19976 cm^{-1} , and the other sub-peaks are blue-shifted with respect to it. It turned out that the overall intensity of this broad peak significantly varied with time, but relative intensities of local peaks within it showed quite small variations. The results for relative intensity of the local peaks we used were obtained by averaging over about 30 recorded spectra. An inspection of the data

collected by *HH*⁵⁶ and *PG*⁵⁷ indicated that these bands could belong to the $B^1\Sigma^+ \rightarrow X^1\Sigma^+$ spectral system of MgO.

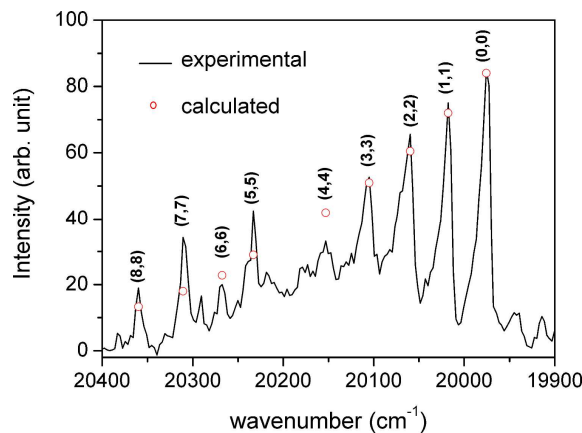


Figure 2.^{104,52} A part of the emission spectrum recorded during PEO of Mg. Anode luminescence contribution is subtracted. The peaks are assigned to (ν', ν'') bands of the $B^1\Sigma^+ \rightarrow X^1\Sigma^+$ band system of MgO. Circles denote intensities of peaks obtained in the simulation procedure described in text.

The most important experimental studies on the $B^1\Sigma^+ - X^1\Sigma^+$ spectral system of MgO were discussed in two of our previous studies.^{104,52} We repeat here the key points.

Ghosh et al.¹⁰⁵ recorded about thirty rotationally unresolved violet-degraded emission bands in the wave number region between 19000 cm^{-1} and 21000 cm^{-1} and assigned them to the sequences $\nu' - \nu'' = 0, \pm 1$, with the vibrational quantum number ν up to ten. Interestingly, neither *HH* nor *PG* cited this important reference. Mahanti⁵⁸ and Lagerqvist and Uhler^{60,103} carried out a vibrational and rotational analysis of the bands of this system and assigned it to $B^1\Sigma^+ - X^1\Sigma^+$. This analysis was confirmed by Pešić,^{64,106} who measured isotopic $^{24}\text{MgO}^{18}/^{26}\text{MgO}^{16}$ shifts. In several studies the rotational constants for the $X^1\Sigma^+$ and $B^1\Sigma^+$ states were precisely determined (Table 3). It has been found that they are very similar in these two electronic states, that for the upper state being slightly larger. Similarity of the equilibrium bond lengths and vibrational frequencies, as well as the fact that the $B - X$ system involves the $^1\Sigma$ species, determines the general features of the spectrum. It is dominated by the $\nu' - \nu'' = 0$ band sequence, the bands have *P* and *R* branches, and the head of each *P* branch is quite far from the corresponding band origin. The position of the band heads ($\tilde{\nu}_h$) with respect to

the band origins ($\tilde{\nu}_0$) can be estimated using the rotational constants $B'' = 0.5743 \text{ cm}^{-1}$ and $B' = 0.5822 \text{ cm}^{-1}$.⁵⁶ By means of the formula (72) we obtain $\tilde{\nu}_h - \tilde{\nu}_0 \cong 40 \text{ cm}^{-1}$.

In Table 4 (Exp. 1) we present the positions of the band heads of the $v' - v'' = 0$ sequence measured by Ghosh et al.¹⁰⁵ The term values relative to the position of the (0-0) band are given in parentheses below the absolute term values. Like in all later studies, these bands were fitted to the formula of type (50), quadratic in the vibrational quantum number. The parameters derived by adapting the original formula by Ghosh et al. to the form (50), as well as the term values computed by means of it, are presented in column Fit 1 of Table 4. The experimental results by Lagerqvist,⁶⁰ and Pešić¹⁰⁶ (for $^{24}\text{Mg}^{18}\text{O}$) are given in columns Exp. 2 and Exp 3, respectively, and those taken by Pearse and Gaydon⁵⁷ from the original references by Mahanti⁵⁸ and Lagerqvist⁶⁰ in column Exp. 4. Pešić¹⁰⁶ fitted the position of both band origins and heads (columns Fit 2 and Fit 3, respectively) using the parameters given on the top of column Fit 3 for origins, and a set of parameters corrected to account for the difference $\tilde{\nu}_h - \tilde{\nu}_0$ for calculating the positions of the band heads. In column Fit 4 are presented the results of calculations of band origins by means of the most reliable set of parameters, adopted by *HH*.⁵⁶ Comparing the results of direct measurements with those obtained by calculating the band positions with the formulae of type (50) we conclude that they agree reasonably with one another only for small vibrational quantum numbers ($v' = v'' \leq 4$). No formula quadratic in the vibrational quantum number v , applied thus far, has given a good reproduction of the measured band positions for higher v values. The explanation of this fact is simple: Looking at the differences in wave numbers of the successive bands observed (e.g. in column Exp. 4) we find that they are 42, 44, 46, 50, 51, 58, and 47 cm^{-1} , i.e. they follow quadratic dependence only for first few terms. This fact will be kept in mind in the following discussion.

The results of our measurements¹⁰⁴ are presented in column Exp 5. The accuracy of the band head positions is estimated to $\pm 5 \text{ cm}^{-1}$. The agreement with the results of previous more precise gas-phase spectral measurements is within this error margin.

Table 4.^{104,52} Positions (in cm^{-1}) of the $v' - v'' = 0$ band heads ($\tilde{\nu}_h$) and origins $\tilde{\nu}_0$ of the B $^1\Sigma^+ - X$ $^1\Sigma^+$ spectral system of MgO. In parentheses are given the term values relative to the position of the 0-0 band.

	Exp.1 a	Exp.2 b	Exp.3 c	Exp.4 d	Exp.5 e	Fit 1 ^a	Fit 2 ^c	Fit 3 ^c	Fit 4 ^c	Fit 5 ^f
\tilde{v}''						721.96		758.38		785.06
$(\omega_e x_e)''$						5.96		4.83		5.18
T_e						19950.2 3		19983.9 6		19984. 0
\tilde{v}'						754.06		796.08		824.08
$(\omega_e x_e)'$						3.06		4.44		4.76
$v'-v''$	\tilde{v}_h	\tilde{v}_h	\tilde{v}_h	\tilde{v}_h	\tilde{v}_h	\tilde{v}_h	\tilde{v}_h	\tilde{v}_0	\tilde{v}_0	\tilde{v}_0
0-0	19966 (0)	19965 (0)	19967 (0)	19971 (0)	19976 (0)	19967 (0)	19966 (0)	20003 (0)	20004 (0)	20004 (0)
1-1	20007 (41)	20007 (42)	20008 (41)	20013 (42)	20018 (42)	20005 (38)	20008 (41)	20241 (38)	20044 (40)	20044 (40)
2-2	20049 (83)	20051 (86)	20049 (82)	20057 (86)	20060 (84)	20049 (82)	20049 (83)	20081 (78)	20084 (81)	20084 (81)
3-3	20093 (127)	20097 (132)	20092 (125)	20103 (132)	20106 (130)	20098 (131)	20092 (125)	20121 (118)	20126 (122)	20127 (123)
4-4	20146 (180)		20137 (170)	20153 (182)	20153 (177)	20153 (186)	20134 (168)	20162 (159)	20168 (164)	20171 (167)
5-5	20200 (234)			20204 (233)	20231 (255)	20215 (248)		20203 (200)	20211 (208)	20216 (213)
6-6	20257 (291)			20262 (291)	20268 (292)	20281 (314)		20245 (243)	20255 (252)	20265 (261)
7-7	20304 (338)			20309 (338)	20310 (334)	20354 (387)		20289 (286)	20300 (297)	20316 (312)
8-8	20347 (381)				20360 (384)	20433 (466)		20333 (330)	20346 (342)	20372 (368)
9-9	20388 (422)					20517 (550)		20377 (374)	20393 (389)	20434 (430)

a: Ref. 105; b: Ref. 60; c: Ref. 106; d: Ref. 57; e: Ref. 56; f: Our study, Refs. 104, 52.

5.3.3. Computation of Franck–Condon factors and vibrational transition moments

In the calculations of the *FCFs* and *VTMs* for the $B^1\Sigma^+ - X^1\Sigma^+$ system of MgO we used a set of experimentally derived molecular parameters⁵⁶ and the *ab initio* computed electric transition function.⁸³ We assumed the potential energy part of the Hamiltonian in the form of a polynomials of third order in the coordinate $x \equiv (r - r_e)$. In this subsection we express the potential energy and the bond length in atomic units ($m_e \equiv 1$, $q_e \equiv 1$, $\hbar \equiv 1$); thus the energy is given in hartree (1 hartree = 27.211 eV) and the bond length in bohr (1 bohr = 0.529177 Å). The force constants k_2 and k_3 are determined as described in subsection 4.4.3. Employing the molecular parameters from Ref. 56 we obtained:

$$\begin{aligned} V(X^1\Sigma^+) &= 0.111991x^2 - 0.07426x^3, \\ V(B^1\Sigma^+) &= 0.0910532 + 0.12331(x + 0.0225)^2 - 0.07844(x + 0.0225)^3, \end{aligned} \quad (73)$$

where $\Delta r_e = -0.0225$ bohr is the difference between the equilibrium bond lengths in the excited and ground electronic state. Based on Fig. 5 of Ref. 83 the electric moment for the transition between the $B^1\Sigma^+$ and $X^1\Sigma^+$ states was assumed in the form

$$R_e(\text{au}) = -1.2 + 0.7x. \quad (74)$$

The vibrational Schrödinger equation corresponding to the potentials (73) was solved variationally, with the basis consisting of eigenfunctions of the harmonic oscillator approximating the $X^1\Sigma^+$ state.

Table 5.^{104,52} *FCFs* (first row for each quantum number v''), and squared *VTMs* (third row) for transitions between vibrational levels of the $X^1\Sigma^+$ and $B^1\Sigma^+$ electronic states of MgO (our study¹⁰⁴). Second row: *FCFs* computed in previous studies.

$v'' \backslash v'$	0	1	2	3	4
0	.9826 .983 ^a	.0170 .017 ^a	.0004 .000 ^a		.0003 ^b
1	1.421 .0173 .017 ^a	.0089 .9464 .948 ^a	.0002 .0351 .033 ^a		.0375 ^b .0011 .001 ^a
2	.0480	1.344 .0364	.0180 .9067	.0001 .0544	.0024

	.035 ^a	.911 ^a	.901 ^b	.053 ^a	.0576 ^b	.0018 ^b
3	.0969	1.263		.0274		.0011
	.0002	.0573		.8632		.0751
	.000 ^a	.053 ^a	.0606 ^b	.881 ^a	.857 ^b	.0804 ^b
4	.0017	.1471		1.179		.0371
		.0005		.0801		.8154
		.0010 ^b		.061 ^a	.0827 ^b	.806 ^b
		.0039		.1981		1.090

a: Ref. 107; b: Ref. 70.

The results for the band origins obtained in these calculations are presented in column Fit 5 of Table 4. For low vibrational quantum numbers ($v' = v'' = 0-3$) they coincide with the numbers in column Fit. 4, generated employing the formula of type (50) with the same set of molecular parameters. The agreement becomes continuously poorer with increasing $v' = v'' \geq 4$, reflecting the restricted reliability of the perturbative approach used to determine the force constants that appear in the formula (73). However, as stated above, the levels with $v' \geq 4$ are in any case unsatisfactorily described by the formulae of type (50) and they were not used for estimation of the plasma temperature.

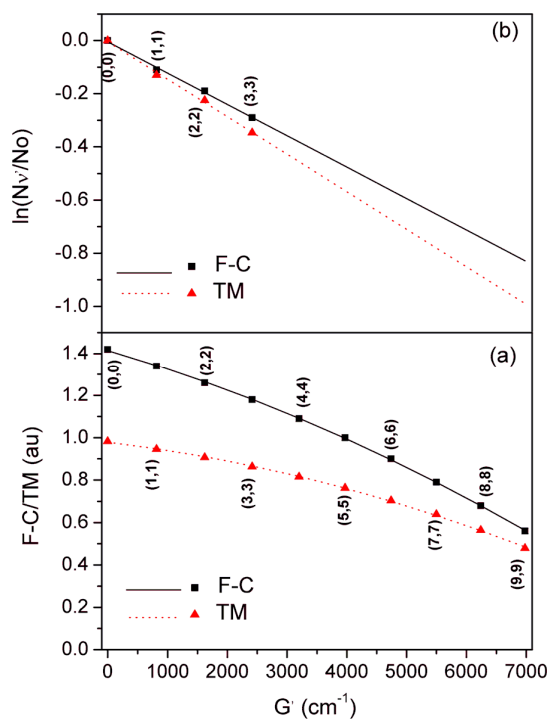


Figure 3.^{104,52} (a) Computed *FCFs* (F–C) and squared *VTMs* (TM) for the ($v' = v''$) bands of the $B^1\Sigma^+ \rightarrow X^1\Sigma^+$ band system of MgO as functions of vibrational term values of the $B^1\Sigma^+$ electronic state; b) logarithm of the relative population of $v' = 0, 1, 2$ and 3 vibrational levels as function of the corresponding term values.

The computed *FCFs* and (squared) *VTMs* (in atomic units) for the levels up to $v = 4$ are given in Table 5. For comparison, we give the *FCFs* computed by Prasad and Prasad¹⁰⁷ and those quoted by Ikeda et al.⁷⁰. Our results either agree well with those from the previous studies or lie between the values published in Refs. 107 and 70. The ratio $|VTM|^2 / FCF$ decreases uniformly with increasing vibrational quantum number within the $v' - v'' = 0$ sequence, reflecting the decrease of the absolute value of the electric transition moment with increasing bond length.

5.3.4. Estimation of vibrational temperature

The relative population of vibrational levels in the $B^1\Sigma^+$ electronic state of MgO, $N_{v'}$, was estimated by means of the procedure described in subsection 4.4.3. We obtained it for the levels $v' = 0 - 3$ as the ratio of the measured intensity of the peaks corresponding to the (0-0), (1-1), (2-2), and (3-3) band heads and the corresponding squared *VTMs*. In Fig. 3b are displayed the values for $\ln(N_{v'}/N_{v'=0})$ as function of the vibrational term values of the $B^1\Sigma^+$ electronic state. If we had a plasma in thermal equilibrium, these points should lie on a straight line, whose slope determines the plasma temperature (as $-hc/kT$). Having in mind that the accuracy of measured relative intensities is roughly 10%, and that the vibrational levels of the $B^1\Sigma^+$ state can also depopulate through transitions to those of the $A^1\Pi$ electronic state (red system of MgO), we considered the deviations of particular points from the straight line in Fig. 3b negligible. Thus, we found it justified to conclude that we have quasi-equilibrium conditions, at least for vibrational motions. The slope of this line corresponds to $T \approx 11500$ K. In Fig. 3b we also present the result obtained when the $|VTM|^2$ are replaced by the corresponding *FCFs*. In this case we obtained $T \approx 9800$ K. The difference between these two temperature values points at the importance of taking into account the variation of the electric transition moment with the bond length. Accounting for the limited accuracy of our

experimental results, as well as of the electric transition moment function employed, we estimated the temperature of our plasma to be $T = 11000 \text{ K} \pm 2000 \text{ K}$. Assuming $T = 11000 \text{ K}$ and using the vibrational transition moments for $v' = v'' = 0-8$, we simulate in Fig. 2 the complete $v' - v'' = 0$ band sequence of the $B^1\Sigma^+ - X^1\Sigma^+$ spectral system of MgO. While some discrepancies between the experimental and simulated results are obvious, the general agreement can be considered as satisfactory.

5.3.5. Estimation of rotational temperature

The plasma temperature was also estimated by means of the emission spectrum of OH.⁵² In the range between 31000 and 33000 cm^{-1} we recorded four groups of unresolved rotational lines with the maxima at 32364 , 32484 , 32597 , and 32622 cm^{-1} . They were assigned to the heads of the Q_2 , Q_1 , R_2 , and R_1 sub-branches corresponding to the $A^2\Sigma^+ (v'=0) - X^2\Pi (v''=0)$ transition (Fig. 4). Employing the approach proposed by de Izarra,¹⁰⁸ we estimated the temperature of $3500\text{K} \pm 500 \text{ K}$. The significant difference between this temperature and that referred in Subsection 5.3.3 could be an indication for non-existence of thermal equilibrium between vibrational and rotational degrees of freedom in our plasma. However, as discussed in Ref. 52, it can also be explained in terms of the two-plasma-zones model, that will be briefly discussed in Conclusions.

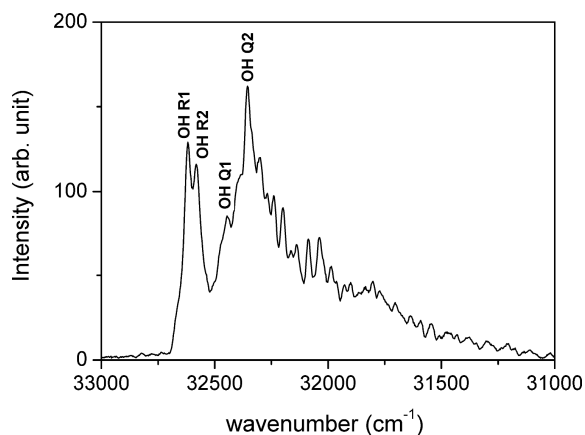


Fig. 4.^{104,52} $A^2\Sigma^+ (v'=0) - X^2\Pi (v''=0)$ luminescence spectrum of OH between 31000 and 33000 cm^{-1} .

6. SPECTRUM OF AIO

6.1. Spectral systems of AIO

The part of the data for AIO we need below, as collected by *HH*,⁵⁶ is presented in Table 6. *HH* constructed this table based on about 50 studies published from 1927 to 1975. All spectra observed until 1975 involved doublet electronic states.

Table 6. A part of the table with molecular constants for $^{27}\text{Al}^{16}\text{O}$ given by *HH*.⁵⁶

State	T_e (cm^{-1})	ω_e (cm^{-1})	$\omega_e X_e$ (cm^{-1})	r_e (\AA)	Observed transitions	ν_{00} (cm^{-1})
$F^2\Sigma^+$	[47677.3]			[1.816 ₄]	$F \rightarrow A$	41843.52 41972.36
$E^2\Delta_i$	45562 45431	(503)		[1.844 ₄]	$E \leftrightarrow A$	39979.81 39977.17
$D^2\Sigma^+$	40266.7	819.6	5.8	1.723 ₄	$(D \rightarrow B)$ $D \leftrightarrow A$	(19552) 34841.23 34970.09
$C^2\Pi_r$	33153 33079	856	6		$D \leftrightarrow X$ $(C \rightarrow B)$ $C \leftrightarrow X$	40187.2 (12457) (12383) 33092 33018
$B^2\Sigma^+$	20688.95	870.05	3.52	1.6670	$B \leftrightarrow X$	20635.22
$A^2\Pi_i$	5470.6 5341.7	728.5	4.15	[1.7708]	$A \leftrightarrow X$	5346 5217
$X^2\Sigma^+$	0	979.23	6.97	1.6179		

*PG*⁵⁷ gave information about six spectral systems of AIO. The green $B^2\Sigma^+ - X^2\Sigma^+$ system, appearing in the wavelength range 541–433 nm, is described in most detail. It was stated that it occurred in a variety of sources including arcs and flames, and that it appeared in form of marked sequences of red-degraded single-headed bands. *PG* presented twenty-one band heads taken from Lagerqvist et al.¹⁰⁹ and Tyte and Nicholls.¹¹⁰ Five ultra-violet spectral systems of AIO were briefly described in the book by *PG*. The information about them was based on Refs. 111–116. These systems occur in emission from arcs, hollow-cathode discharges, and microwave excitation. The bands of the $C^2\Pi - X^2\Sigma^+$ (extended from 332 to

287 nm), $E^2\Sigma^+ - A^2\Pi$ (around 250 nm), $D^2\Sigma^+ - X^2\Sigma^+$ (280–230 nm), and $F^2\Pi - A^2\Pi$ (at 238.0 nm) systems are degraded to the red, and are double-headed, except of the $F^2\Pi - A^2\Pi$, which are double double-headed). The bands of the $D^2\Sigma^+ - A^2\Pi$ system (300–280 nm) are double-headed and degraded to the violet.

Comparing the data collected by *HH* and *PG*, we state that *HH* included in their book the $A^2\Sigma^+ - X^2\Sigma$ systems in the (infra-red) region at about 1900 nm, only indirectly mentioned by *PG*. The reason might be that the first reference¹¹⁷ used by *HH* appeared between third and fourth edition of *PG*'s book, and the second one¹¹⁸ even later.

The third comprehensive source of literature data on the spectra of AIO represents the theoretical paper by Zenouda et al.¹¹⁹ The electronic ground state was well characterized by infra-red optical double resonance spectroscopy,¹²⁰ by purely rotational transitions^{121–123} and fine structure splitting.¹²⁴ The infra-red $A^2\Sigma^+ - X^2\Sigma^+$ system was used to determine accurate spectroscopic constants for both electronic species in question.^{125–128} The blue-green $B^2\Sigma^+ - X^2\Sigma^+$ system was investigated in Refs. 128–135. Precise rotational constants were determined¹³² for many vibrational levels. A series of studies were devoted to the $C^2\Sigma^+ - X^2\Sigma^+$ system.^{136–141} The systems $D^2\Sigma^+ - X^2\Sigma^+$,¹³⁶ $C^2\Pi - A^2\Pi$,^{137,138} $D^2\Sigma^+ - A^2\Pi$,¹³⁹ and $E^2\Delta - A^2\Pi$ ¹³⁶ were also investigated. Low-lying electronic states of AIO were studied by photoelectron spectroscopy, too.^{142,143} Potential energy functions for the $X^2\Sigma^+$, $A^2\Pi$, $X^2\Sigma^+$, $B^2\Sigma^+$, and $D^2\Sigma^+$ states and *FCFs* for the corresponding transitions were computed by means of the RKR method.^{133,144,145}

6.2. Quantum chemical studies on AIO

The early *ab initio* calculations on the AIO molecule^{146–151} were carried out employing similar approaches and presented the results of similar type (equilibrium geometries, vibrational frequencies, excitation energies, transition moments) as their MgO counterparts.^{75,82–96} We skip immediately to the benchmark study by Zenouda et al.¹¹⁹ Like the study by Maatouk et al.⁸³ on MgO, it was carried out using the MOLPRO program package⁹⁷ in its somewhat older performance. The computations were performed at the CASSCF and the MRCI level of sophistication, involving basis sets of quintuple zeta quality.⁹⁹ The potential curves and electric dipole/transition moments for the ground state and all doublet and quartet

excited states up to 50000 cm^{-1} were calculated. We concentrate on the states we are interested in, namely on $X^2\Sigma^+$, $B^2\Sigma^+$, and $C^2\Pi$.

The completely populated 1s, 2s, 2p AOs of Al and 1s, 2s of O build the molecular orbitals (MOs) 1σ – 5σ , and 1π of AlO. These orbitals are found to be completely populated in all Slater determinants significantly contributing to the electronic states computed in the framework of the study. As expected, the most important role in building of lower-lying (i.e. up to 50000 cm^{-1}) states of AlO play the MOs involving the 3s, 3p AOs of Al and 2p of O. The seven AOs, $3s_\sigma$, $3p_\sigma$, $3p_\pi$ of Al and $2p_\sigma$, $2p_\pi$ of O built the next four σ and two π orbitals. It was found that the most important electron configurations are those in which seven valence electrons (three originating from the Al atom, and four from oxygen) are distributed among the following MOs: the 6σ bonding orbital, built by the $2p_\sigma$ AO of oxygen and admixed by $3s$ and $3p_\sigma$ of Al; the 2π orbital representing mainly the $2p_\pi$ orbital of oxygen; the non-bonding 7σ orbital being a combination of the $3s$ and $3p$ orbitals of Al; the 3π orbital built predominantly by $3p_\pi$ orbital of Al.

The dominant configurations for the $X^2\Sigma^+$ and $B^2\Sigma^+$ electronic states are $6\sigma^2 2\pi^4 7\sigma^1$ ($\text{Al}^{2+}\text{O}^{2-}$) and $6\sigma^1 2\pi^4 7\sigma^2$ and $6\sigma^2 2\pi^3 7\sigma^1 3\pi^1$ (Al^+O^-). The two main configurations for the $D^2\Sigma^+$ state are $6\sigma^2 2\pi^3 7\sigma^1 3\pi^1$ and $6\sigma^2 2\pi^4 8\sigma^1$. The main configuration for the $A^2\Pi$ state is $6\sigma^2 2\pi^3 7\sigma^2$. The $C^2\Pi$ state is strongly multiconfigurational with two dominant configurations $6\sigma^2 2\pi^4 3\pi^1$ and $6\sigma^1 7\sigma^1 2\pi^4 3\pi^1$. The main configuration of the $C'^2\Pi$ state is $6\sigma^2 2\pi^2 7\sigma^2 3\pi^1$. A consequence of an avoided crossing between the C and C' states is an energy barrier of 0.68 eV above the dissociation asymptote for the $C^2\Pi$ state. Zenouda et al. claimed that this fact explained why excited vibrational levels up to $v' = 10$ had been observed,¹³⁸ even though the highest of them are located above the dissociation limit.

In the F–C region, the largest electric transition moment involving these species is that for the $X^2\Sigma^+ - B^2\Sigma^+$ transition. It was found to be between approximately 0.7 and 0.4 a.u. in a rather broad F–C region; it decreases with increasing bond length, becoming negligible when the Al–O distance overestimates by roughly 1 Å its equilibrium value. The electric moment for the $C^2\Pi - X^2\Sigma^+$ transition was found to be fairly large (0.5 a.u.), indeed like all those involving the ground and the low-lying excited doublet electronic states.

The results of the *ab initio* study by Zenouda et al. are compared in Table 7 with the corresponding experimental findings.

Table 7. Comparison of theoretical¹¹⁹ and experimentally derived molecular structure parameters for doublet electronic states of AlO.

State	T_e (cm^{-1})	$(T_e)_{\text{exp}}$ (cm^{-1})	ω_e (cm^{-1})	$(\omega_e)_{\text{ex}}$ _p (cm^{-1})	$\omega_e x_e$ (cm^{-1})	$(\omega_e x_e)_{\text{exp}}$ (cm^{-1})	r_e (\AA)	$(r_e)_{\text{exp}}$ (\AA)
$F^2\Sigma^+$	48895	47677 ^a	850				1.78	1.816 ^a
$C^2\Pi$	47380		770				2.19	
$e^4\Pi$	47320		590				1.79	
$E^2\Sigma^-$	47225		490				1.865	
$E^2\Delta$	46250	45431 ^b	496	503 ^b			1.858	1.844 ^b
$d^4\Pi$	41190		768				1.72	
$D^2\Sigma^+$	40685	40268 ^c	833	817.5 ^c			1.726	1.727 ^c
$C^2\Pi$	32875	33108 ^d	846	856 ^e			1.679	1.671 ^d
$G^2\Sigma^-$	32351		716				1.791	
$G^2\Delta$	31852		719				1.786	
$c^4\Sigma^-$	30678		690				1.788	
$b^4\Delta$	29350		699				1.785	
$a^4\Sigma^+$	27222		723				1.776	
$B^2\Sigma^+$	20192	20689 ^f	869	870.44 ^f	4.18	3.668 ^f	1.677	1.667
$A^2\Pi$	5050	5460 ^g	720	729.7 ^g	4.18	4.88 ^g	1.777	1.7678 ^g
$X^2\Sigma^+$	0	0	977	979.5 ^g	6.8	7.08 ^g	1.623	1.6179 ^g

^a Ref. 114; ^b Ref. 136; ^c Ref. 115; ^d Ref. 140; ^e Ref. 111; ^f Ref. 132; ^g Ref. 127.

6.3. $B^2\Sigma^+ \rightarrow X^2\Sigma^+$ spectral system of AlO

6.3.1. Rotational structure of the electronic transition

In multiplet Σ electronic states ($\Lambda = 0$, $S \neq 0$) we have also the spin-rotation coupling; we add then to the Hamiltonian (24/25) the operator (26). Thus we are dealing with

$$\hat{H}_{rot} + \hat{H}_{SR} = \frac{B}{\hbar^2} \hat{N}^2 + \frac{\gamma}{\hbar^2} \left(\hat{N} \cdot \hat{S} \right) \quad (75)$$

Since this operator only involves the scalar products operators, the Hamiltonian is so symmetric that the *SFS* and *MFS* are equally appropriate for working. We choose the *SFS* to avoid any complications caused by anomalous commutation relations. We use here the Hund's case (b) basis functions (33). In view of Eq. (37), each individual of them has a definite parity, being $(-1)^N$ for Σ^+ , and $(-1)^{N+1}$ for Σ^- electronic states. In this basis the first operator on the right-hand side of Eq. (75) has only diagonal matrix elements equal $BN(N+1)$. To calculate the matrix elements of the second operator, we use the relation

$$\hat{J}^2 = \left(\hat{N} + \hat{S} \right)^2 = \hat{N}^2 + \hat{S}^2 + 2\hat{N} \cdot \hat{S}, \quad (76)$$

and transform the second operator on the right-hand side of Eq. (75) into

$$\frac{\gamma}{\hbar^2} \left(\hat{N} \cdot \hat{S} \right) = \frac{\gamma}{2\hbar^2} \left(\hat{J}^2 - \hat{N}^2 - \hat{S}^2 \right). \quad (77)$$

Also this operator is diagonal in the chosen basis. Its matrix elements are $\gamma[J(J+1) - N(N+1) - S(S+1)]/2$. For each value of the quantum number N there are two close-lying levels of the same parity, corresponding to $J = N \pm 1/2$. The $J = N + 1/2$ and $J = N - 1/2$ levels are called F_1 and F_2 , respectively. Their term values are

$$\tilde{\nu}(J = N + 1/2) = B(J - 1/2)(J + 1/2) + \frac{1}{2}\gamma(J - 1/2) = BN(N + 1) + \frac{1}{2}\gamma N, \quad (78)$$

and

$$\tilde{\nu}(J = N - 1/2) = B(J + 1/2)(J + 3/2) - \frac{1}{2}\gamma(J + 3/2) = B_v N(N + 1) - \frac{1}{2}\gamma(N + 1). \quad (79)$$

The magnitude of the splitting (except for the $N = 0, J = \pm 1/2$ level that is not split) is

$$\tilde{\nu}(J = N + 1/2) - \tilde{\nu}(J = N - 1/2) = (N + 1/2)\gamma. \quad (80)$$

This shows that the magnitude of the spin-rotation splitting linearly increases with N .

The selection rule for rotational transitions when both electronic states are of $^2\Sigma$ symmetry is the same as for $^1\Sigma - ^1\Sigma$ electronic transitions, namely $J = J' + 1$ („ R branch“) and $J = J' - 1$ („ P branch“). Additionally, we have here not strict, but very pronounced $N' = N'' \pm 1$ selection rule. In the case $B \ ^2\Sigma^+ \rightarrow X \ ^2\Sigma^+$ electronic transition of AlO, we have $B' < B''$ and thus red degraded bands with the head in the R -branch at (see Eq. 69)

$$J_h = \frac{3B' - B''}{2(B'' - B')} \quad (81)$$

and

$$\tilde{\nu}_h - \tilde{\nu}_0 = 2B' + \frac{(3B' - B'')^2}{4(B' - B'')}. \quad (82)$$

6.3.2. Identification of bands

In our recent study on Al ¹⁵² we investigated the emission spectrum recorded in the wave number range between 18000 and 20000 cm^{-1} . It consisted of two broad peaks with clearly pronounced structure, extending from roughly 18200 to 18800 cm^{-1} and from 19000 to 19700

cm^{-1} with the maxima at approximately 18500 and 19500 cm^{-1} , respectively. Thus, they appeared in the spectral region where the appearance of the bands of the $B^2\Sigma^+ - X^2\Sigma^+$ emission transition of AlO was expected. We estimated the uncertainty of measured spectral lines/peak maxima to be 5 cm^{-1} , and of their relative intensities (after subtracting the anodic luminescence contribution) to roughly 10%.

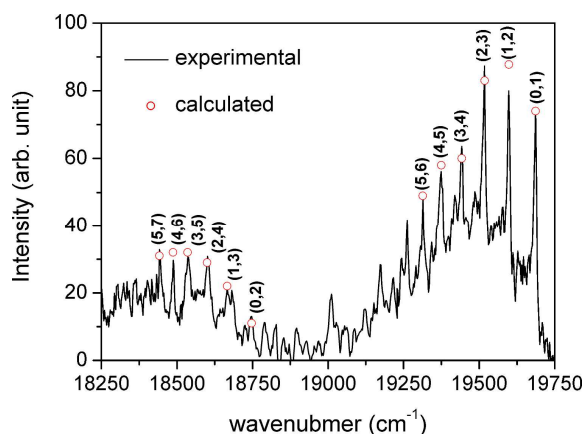


Figure 5¹⁵² A part of the emission spectrum recorded during PEO of Al. Anode luminescence contribution is subtracted. The peaks are assigned to $v'-v'' = -1$ and -2 band sequences of the $B^2\Sigma^+ \rightarrow X^2\Sigma^+$ system of AlO. Circles denote intensities of peaks obtained in the simulation procedure described in text.

In order to assign the observed spectral features, we constructed a Deslandres table for the $B^2\Sigma^+ - X^2\Sigma^+$ system of AlO (Table 8). We used for that the band origins published by Saksena *et al.*¹³⁵ Using the rotational constants from that reference, $B'' = 0.64165$ and $B' = 0.60897$, and Eq. (81), with J replaced by N [see Eqs. (78/79) for $^2\Sigma$ states], we estimated in the lowest-order approximation the quantum number N corresponding to the head of the R branch to be 18. The position of the band head with respect to the band origin is thus, according to Eq. (82), about 12 cm^{-1} blue-shifted. At our resolution of the spectrum we did not observe the spin-rotation splitting, Eq. (80).

Table 8. The band positions (in cm^{-1}) of the green system, $B^2\Sigma^+ - X^2\Sigma^+$ of AlO. The term values, $T_{v''}$, $T_{v'}$ are taken from ref. 135 (we completed these results with the values labeled by asterisk). The numbers with superscript 0 represent the positions of the band origins, and

those with superscript *h* of the recorded band heads (mean values for R_1 and R_2 sub-branches). The numbers without superscript are the band positions measured in our study.¹⁵²

T_v	v	20635 ⁰	21498 ⁰	22354 ⁰	23203 ⁰	24044 ⁰	24877 ⁰	25704 ⁰	26523 ⁰	27335 ⁰	28139 ⁰
T_v	v	0	1	2	3	4	5	6	7	8	9
0 ⁰	0	20635 ⁰ 20646 ^h 20640	21498 ⁰ 21508 ^h 21500	22354 ⁰ 22362 ^h	23203 ⁰	24044 ⁰	24877 ⁰	25704 ⁰	26523 ⁰	27335 ⁰	28139 ⁰
965 ⁰	1	19670 ⁰ 19682 ^h 19680	20533 ⁰ 20544 ^h 20550	21389 ⁰ 21398 ^h 21390	22237 ⁰ 22246 ^h	23078 ⁰	23912 ⁰	24738 ⁰	25558 ⁰	26369 ⁰	27174 ⁰
1917 ⁰	2	18718 ⁰ 18733 ^h 18730	19582 ⁰ 19594 ^h 19590	20437 ⁰	21286 ⁰ 21295 ^h	22127 ⁰ 22135 ^h	22961 ⁰	23787 ⁰	24606 ⁰	25418 ⁰	26222 ⁰
2854 ⁰	3	17781 ⁰ 18658 ⁰	18644 ⁰ 18660 ^h 18660	19500 ⁰ 19513 ^h 19510	20348 ⁰	21189 ⁰ 21199 ^h 21190	22023 ⁰ 22032 ^h	22850 ⁰	23669 ⁰	24481 ⁰	25285 ⁰
3778 ⁰	4	16858 ⁰	17721 ⁰	18577 ⁰ 18593 ^h 18590	19425 ⁰ 19439 ^h 19435	20266 ⁰ 20270	21100 ⁰	21926 ⁰ 21935 ^h	22746 ⁰	23557 ⁰	24362 ⁰
4687 ⁰	5	15949 ⁰	16812 ⁰	17667 ⁰	18516 ⁰ 18533 ^h 18530	19357 ⁰ 19371 ^h 19365	20191 ⁰	21017 ⁰	21836 ⁰	22648 ⁰	23453 ⁰
5582 ⁰	6	15053 ⁰	15916 ⁰	16772 ⁰	17624 ⁰	18462 ⁰ 18480 ^h 18475	19296 ⁰ 19310 ^h 19305	20122 ⁰	20941 ⁰	21753 ⁰	22557 ⁰
6463 ⁰	7	14172 ⁰	15035 ⁰	15891 ⁰	16739 ⁰	17581 ⁰	18414 ⁰ 18435 ^h 18430	19241 ⁰ 19257 ^h 19250	20060 ⁰	20872 ⁰	21676 ⁰
7330 ^{0*}	8	13305 ^{0*}	14168 ^{0*}	15024 ^{0*}	15873 ^{0*}	16714 ^{0*}	17547 ^{0*}	18374 ^{0*}	19193 ^{0*}	20005 ^{0*}	20809 ^{0*}
8183 ^{0*}	9	12452 ^{0*}	13315 ^{0*}	14171 ^{0*}	15020 ^{0*}	15861 ^{0*}	16694 ^{0*}	18385 17521 ^{0*}	19205 18340 ^{0*}	19152 ^{0*}	19956 ^{0*}
9023 ^{0*}	10	11612 ^{0*}	12475 ^{0*}	13331 ^{0*}	14180 ^{0*}	15021 ^{0*}	15854 ^{0*}	16681 ^{0*}	18350 17500 ^{0*}	19160 18312 ^{0*}	19116 ^{0*}
9848 ^{0*}	11	10787 ^{0*}	11650 ^{0*}	12506 ^{0*}	13355 ^{0*}	14196 ^{0*}	15029 ^{0*}	15856 ^{0*}	16675 ^{0*}	18320 17487 ^{0*}	19115 18291 ^{0*}
											18295

We completed the data from Table 3 of the original reference¹³⁵ by computing the term values for the quantum numbers $v'' = 8-11$ by means of the molecular parameters from Table 5 of that paper. The positions of the experimentally observed band heads (mean values for the R_1/R_2 branches) are also presented in Table 8. The results of our study match very reasonably the $v'-v'' = -1$ and -2 sequences of the $B^2\Sigma^+ - X^2\Sigma^+$ system. Moreover, we detected several bands $[(v', v'') = (7,8), \dots, (11,12)$ and $(6,8), \dots, (10,12)$; not all of them are presented in Table 8] that have not been analyzed experimentally thus far. They involve the ground state levels $v'' = 8-12$ which were suspected to be heavily perturbed and/or predissociated.^{109,135,153}

6.3.3. Computation of Franck–Condon factors and vibrational transition moments

The *FCFs* for the transitions between vibrational levels of the $B^2\Sigma^+$ and $X^2\Sigma^+$ electronic states of AlO have been computed in several studies. A comparison of the results obtained by various authors was made in a study by Londhe et al.¹⁴⁵ However, only the study by Sato et al.¹³⁴ addressed the problem of variation of the electric transition moment with the bond length. The authors found that the electric moment for the transition between these two species dramatically decreases with the elongation of the Al–O bond. This conclusion was confirmed in *ab initio* calculations by Zenouda et al.¹¹⁹.

We calculated the *FCFs* and *VTMs* for the $B^2\Sigma^+ - X^2\Sigma^+$ system of AlO in the same way as for the $B^1\Sigma^+ - X^1\Sigma^+$ system of MgO, using a set of experimentally derived molecular parameters¹³² and the *ab initio* computed electronic transition function.¹¹⁹ The results of our calculations of the *FCFs* and squared *VTMs* (in atomic units) for the bands we are interested in are presented in Table 9 and Fig. 6(a). For comparison, we give in column *FCF_{exp}* the *FCFs* computed by Londhe et al.¹⁴⁵. The agreement between these results and ours is quite good (two slightly different sets of molecular parameters are used in these two studies).

Table 9.¹⁵² $v'-v'' = -1$ and -2 sequences of the $B^2\Sigma^+ - X^2\Sigma^+$ luminescence spectrum of AlO. *T*: Band positions measured in our study [152]. *FCF*: Franck–Condon factors computed in the present study by employing molecular parameters from Ref. 132. *FCF_{exp}*: F–C factors published in Ref. 145. $|VTM|^2$: Vibrational transition moments (squared) computed using molecular parameters from Ref. 132 and *ab initio* computed electronic transition moment function.¹¹⁹ *I*: Measured band intensities (in arbitrary units).

ν', ν''	T	FCF	FCF_{exp}	$ VTM ^2$	I	I/FCF	I/FCF_{exp}	I/VTM
0,1	19680	.235	.243	.112	74	315→1.00	305→1.00	660→1.00
1,2	19590	.3315	.352	.1545	81	244→.77	230→.75	524→.79
2,3	19510	.357	.384	.162	86	241→.76	224→.73	530→.80
3,4	19435	.352	.373	.155	63	179→.57	169→.55	406→.62
4,5	19365	.340	.342	.1445	56	165→.52	164→.54	388→.59
5,6	19305	.332	.304	.1355	47	141→.45	155→.51	347→.53
6,7	19250							
7,8	19205							
8,9	19160							
9,10	19115							
0,2	18730	.0354	.032	.0151	11	311→1.00	344→1.00	728→1.00
1,3	18660	.0806	.077	.0334	20	248→.80	260→.76	599→.82
2,4	18590	.124	.126	.0496	30	242→.78	238→.69	605→.83
3,5	18530	.160	.171	.0618	30	187→.60	175→.51	485→.67
4,6	18475	.189	.211	.0695	30	159→.51	142→.41	432→.59
5,7	18430	.208	.245	.0725	31	149→.48	127→.37	427→.59
6,8	18385							
7,9	18350							
8,10	18320							
9,11	18295							

6.3.4. Estimation of vibrational temperature

In the last three columns in Table 9 are presented the ratios of the measured intensity of bands (in arbitrary units) and the computed $FCFs$ and squared $VTMs$. These numbers should be proportional to the population of the vibrational levels of the $B^2\Sigma^+$ state. If our approach is correct, they should be equal for the transitions $\nu'-\nu'' = -1$ and $\nu'-\nu'' = -2$ with the same quantum number ν' . We find the agreement between both sets of results satisfactory [e.g. for the $\nu', \nu'' = 0,1$ and $0,2$ bands we have 315 versus 311 ($FCFs$, this study) 305 versus 344 (FCF_{exp}), and 660 versus 728 (VTM)]. In Table 9 are also presented the values for I/FCF and $I/|VTM|^2$ normalized to one for the $\nu', \nu'' = 0,1$ and $0,2$ transitions. These numbers should correspond to relative population of the excited vibrational ν' levels with respect to the $\nu' = 0$ one, $N_{e,\nu'} / N_{e,0}$. They are presented graphically in Fig. 6a.

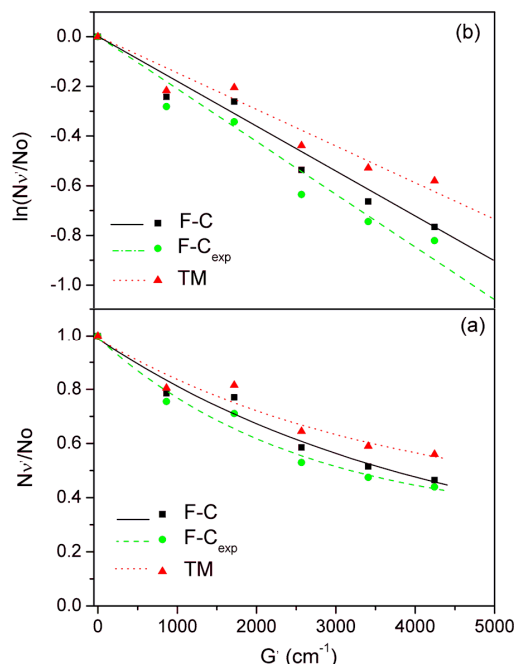


Figure 6.¹⁵² (a) Computed relative population of $v' = 0, 1, 2, 3, 4,$ and 5 vibrational levels (from left to right) of the $B^2\Sigma^+$ electronic state of AlO. Measured intensity distributions within recorded band progressions are combined with the *FCFs* (F–C) and *VTMs* (TM) calculated in our study 152, as well as with the *FCFs* (FCF_{exp}) published in Ref. 145. (b) Logarithm of the relative population of $v' = 1, \dots, 5$ vibrational levels as function of the corresponding term values. For detailed explanation see text.

Assuming again the existence of partial (vibrational) thermal equilibrium, we can extract from the above results the value for the mean temperature of our plasma. In Fig. 6b are displayed the values for $\ln(N_{e_{v'}} / N_{e_0})$ as functions of the vibrational term values (G) of the $B^2\Sigma^+$ electronic state. In spite of some deviations of the points from the straight lines in Fig. 6b, one can extract quite unambiguously three temperature values: $T \approx 8000$ K (*FCF* data), $T \approx 6800$ K (*FCF_{exp}* data), and $T \approx 9400$ K (*VTM* data). The differences in the F–C factors computed in the present study and those published by Londhe et al.¹⁴⁵ cause a discrepancy between the corresponding temperatures of over 1000 K. On the other hand, when the variation of the electronic transition moment with the bond length is taken into account, the estimated temperature is almost 1500 K higher than that obtained by neglecting this dependence. If this dependence was combined with the F–C factors by Londhe et al., we

would again obtain the temperature value of roughly 8000 K. Since we were not able to decide unambiguously which of these three results is the most correct one, we found it correct to conclude that the mean temperature of our plasma is $T = 8000 \pm 2000$ K. In Fig. 5 we present the intensity distribution simulated by employing the temperature value of 8000 K and the *FCFs* computed in the present study (circles). Similar simulated spectrum is obtained when instead of the *FCFs* the *VTMs* combined with $T = 9400$ are employed.

Let us note that the above vibrational temperatures are very similar to the temperature we obtained very recently (the results are not yet published) employing several atomic lines of Al. This is an indication that the concept of partial “local thermal equilibrium” can be extended such that we can speak about “local thermal equilibrium” that involves at least vibrational and (electron) excitation modes.

6.4. $C^2\Pi \rightarrow X^2\Sigma^+$ system of AlO

6.4.1. Rotational energy levels and wave functions of $^2\Pi$ electronic states

Spatially degenerate electronic states ($\Lambda \neq 0$) introduce a new element in play: the molecular axis (z) as an distinguished direction in space. The molecular axis does, of course, exist in Σ electronic states too, but its presence is not reflected in the form of the rotation Hamiltonian when it is written in the convenient (isomorphic) form. However, in spatially degenerate electronic states the presence of axially symmetric (with respect to the molecular axis) electrostatic field has a consequence that some of the projections of particular angular momenta on the molecular axis represent constants of motion, i.e. that the corresponding quantum numbers are at least nearly „good“. This always concerns the projection Λ of the electronic angular momentum \hat{L} . On the other hand, the projections of \hat{L} along the axes perpendicular to the molecular axis, are completely undetermined and their mean values equal zero.

In a $^2\Pi$ state, $\Lambda = \pm 1$, $S = 1/2$, so that $\Sigma = \pm 1/2$. Hence Ω can take the values $-3/2, -1/2, 1/2, 3/2$. Except for the $J = 1/2$ level (which can be exclusively associated with $|\Omega| = 1/2$) each J level has four associated rotational sublevels, two of each parity. We use the simplified rotational Hamiltonian (25) plus the spin-orbit operator (28). Thus, we neither consider the Λ -splitting, nor the spin-rotation coupling, being in the concrete case ($C^2\Pi$ of

AIO) we handle a much weaker effect, than the spin-orbit coupling. We will express the Hamiltonian in terms of the components of angular momenta along the *MFS*-axes, because this coordinate system is obviously more natural when the presence of the internuclear axis plays any role. This Hamiltonian will be partitioned as $\hat{H} = \hat{H}_1 + \hat{H}_2$, where \hat{H}_1 is the dominating part. Its form will depend on whether the spin-orbit coupling is so strong to force the spin to be tied to the molecular axis [Hund's case (a)], or the effect of the rotation is stronger, so that the spin is torn off the molecular axis and is freely oriented in space [Hund's case (b)]. We shall choose as the basis for the representation of the complete Hamiltonian the eigenstates of \hat{H}_1 . Of course, the eigenvalues of the total Hamiltonian do not depend on the choice of the basis. However, if we succeed to carry out a sensible partitioning of the Hamiltonian, its matrix representation will be characterized by relatively small off-diagonal elements and the calculation of the matrix elements will be easier.

a) Hund's case (a)

When the spin-orbit coupling is strong, i.e. at $|A_{SO}| \gg B$, it is natural to partition the Hamiltonian in the following way:

$$\begin{aligned} \hat{H}_R &= H_1 + \hat{H}_2, \\ \hat{H}_1 &= \frac{B}{\hbar^2} (\hat{J}^2 + \hat{S}^2 - \hat{L}_z^2) - \frac{2B}{\hbar^2} \hat{J}_z \hat{S}_z + \frac{A_{SO}}{\hbar^2} \hat{L}_z \hat{S}_z, \quad \hat{H}_2 = -\frac{B}{\hbar^2} (\hat{J}_+^m \hat{S}_-^m + \hat{J}_-^m \hat{S}_+^m). \end{aligned} \quad (83)$$

The complete Hamiltonian (83) commutes with the operators \hat{J}^2 , \hat{S}^2 , and \hat{L}_z , and its dominant part, \hat{H}_1 additionally with the *z*-components of the spin and total angular momentum operator, \hat{S}_z and \hat{J}_z , respectively. Thus we have three good quantum numbers, J, S , and Λ , and nearly good quantum numbers Σ (for \hat{S}_z) and $\Omega = \Lambda + \Sigma$ (for \hat{J}_z). We can use as basis functions:

$$\begin{aligned} |-3/2\rangle &\equiv |-1\rangle |S, -1/2\rangle |J, -3/2\rangle, \quad |-1/2\rangle \equiv |-1\rangle |S, 1/2\rangle |J, -1/2\rangle, \\ |1/2\rangle &\equiv |1\rangle |S, -1/2\rangle |J, 1/2\rangle, \quad |3/2\rangle \equiv |1\rangle |S, 1/2\rangle |J, 3/2\rangle, \end{aligned} \quad (84)$$

where $S = 1/2$ (the symbols n, v, M are omitted).

The dominant part of the Hamiltonian, \hat{H}_1 , has in the chosen basis only diagonal elements. On the other hand, the operator \hat{H}_2 has only the off-diagonal non-vanishing matrix elements $\langle \mp 3/2 | \hat{H}_2 | \mp 1/2 \rangle$. Thus the Hamiltonian matrix has a block structure with two

identical 2×2 blocks, one involving the basis functions $|-3/2\rangle$ and $|-1/2\rangle$, and the other with $|3/2\rangle$ and $|1/2\rangle$. The same block-structure is obtained when instead of the basis functions (84) their parity adapted linear combinations,

$$\begin{aligned} |^2\Pi_{1/2}; J, \pm\rangle &= \frac{1}{\sqrt{2}} \{ |1\rangle |S, -1/2\rangle |J, 1/2\rangle \pm |-1\rangle |S, 1/2\rangle |J, -1/2\rangle \}, \\ |^2\Pi_{3/2}; J, \pm\rangle &= \frac{1}{\sqrt{2}} \{ |1\rangle |S, 1/2\rangle |J, 3/2\rangle \pm |-1\rangle |S, -1/2\rangle |J, -3/2\rangle \}, \end{aligned} \quad (85)$$

are used. Both the + and – parity sub-blocks of the Hamiltonian matrix have the structure,

$$\begin{pmatrix} B[J(J+1) - 7/4] + A_{SO}/2 & -B\sqrt{J(J+1) - 3/4} \\ -B\sqrt{J(J+1) - 3/4} & B[J(J+1) + 1/4] - A_{SO}/2 \end{pmatrix}, \quad (86)$$

The eigenvalues (in cm^{-1}) of the Hamiltonian are

$$\tilde{\nu}_{1/2} = B[J(J+1) - \Lambda^2 + 1/4] \pm \sqrt{B^2(J+1/2)^2 - BA_{SO} + (A_{SO}/2)^2}. \quad (87)$$

The + and – signs in Eq. (87) correspond to the F_2 and F_1 levels, respectively. Their eigenfunctions are⁴³

$$|\psi(F_2)\rangle = a_J |^2\Pi_{3/2}, J, \pm\rangle - b_J |^2\Pi_{1/2}, J, \pm\rangle, \quad |\psi(F_1)\rangle = b_J |^2\Pi_{3/2}, J, \pm\rangle + a_J |^2\Pi_{1/2}, J, \pm\rangle, \quad (88)$$

where

$$a_J = \frac{1}{\sqrt{2}} \sqrt{1 + \frac{A_{SO} - 2B}{\sqrt{4B^2(J+1/2)^2 - 4BA_{SO} + A_{SO}^2}}}, \quad b_J = \frac{1}{\sqrt{2}} \sqrt{1 - \frac{A_{SO} - 2B}{\sqrt{4B^2(J+1/2)^2 - 4BA_{SO} + A_{SO}^2}}} \quad (89)$$

When (absolute value of) the spin–orbit constant is assumed to be much larger than the rotation constant, i.e. $B/|A_{SO}| \ll 1$ [Hund’s case (a)] – we consider first the “regular” situation, when $A_{SO} > 0$ – the energy values up to the first order in this ratio are:

$$\begin{aligned} \tilde{\nu}_{J, \Omega=3/2} &\cong B[J(J+1) - (\Lambda|+1/2|^2)] + \frac{A_{SO}}{2} + \frac{B}{2} = B[J(J+1) - \Omega_{|\Lambda|+1/2}^2] + \frac{A_{SO}}{2} + \frac{B}{2}, \\ \tilde{\nu}_{J, \Omega=1/2} &\cong B[J(J+1) - (\Lambda|-1/2|^2)] - \frac{A_{SO}}{2} + \frac{B}{2} = B[J(J+1) - \Omega_{|\Lambda|-1/2}^2] - \frac{A_{SO}}{2} + \frac{B}{2}. \end{aligned} \quad (90)$$

The term $B/2$, not depending on J can be neglected. Thus in the first approximation each rotation level is split into two levels separated from each other by A_{SO} . For the “inverted” case, $A_{SO} < 0$, the energy ordering of the $\Omega=3/2$ and $\Omega=1/2$ levels is reversed. When $|A_{SO}| \gg B$, we have $a_J \cong 1$ and $b_J \cong 0$ (at $A_{SO} > 0$), or $a_J \cong 0$ and $b_J \cong 0$ (at $A_{SO} < 0$). In this case we can assign the F_2 and F_1 levels as belonging to separate $^2\Pi_{3/2}$ and $^2\Pi_{1/2}$ states.

It is for this situation that Ω is practically a good quantum number. The coupling scheme of the angular momenta can be understood in terms of two phases: The orbit and spin angular momenta couple first into the total electronic angular momentum, \hat{J}_e , and then \hat{J}_e couples with the angular momentum of the nuclear rotation \hat{R} giving the total angular momentum \hat{J} .

In the other extreme case, when the spin-orbit constant is much smaller than the rotational constant [as mentioned above, from the spectroscopic point of view, in this case Hund's scheme (a) is not convenient], i.e. at $|A_{so}|/B \ll 1$, we have in the first approximation

$$\begin{aligned}\tilde{v}_{N=J+1/2} &\cong B[(J+1/2)(J+3/2)-1] - \frac{A_{so}}{2(J+1/2)} = B[N_{J+1/2}(N_{J+1/2}+1) - \Lambda^2] - \frac{\Lambda^2 A_{so}}{2N_{J+1/2}}, \\ \tilde{v}_{N=J-1/2} &\cong B[(J-1/2)(J+1/2)-1] + \frac{A_{so}}{2(J+1/2)} = B[N_{J-1/2}(N_{J-1/2}+1) - \Lambda^2] + \frac{\Lambda^2 A_{so}}{2(N_{J-1/2}+1)}.\end{aligned}\quad (91)$$

In this case the eigenfunction (88) involve appreciable contributions of both $|^2\Pi_{3/2}, J, \pm\rangle$ and $|^2\Pi_{1/2}, J, \pm\rangle$ basis functions, and at high rotation quantum numbers J , $a_j \cong b_j \rightarrow 1/\sqrt{2}$.

Since [see Eqs. (91)] the contribution of the spin-orbit operator (28) to the energy becomes continuously smaller at increasing J , the spin-rotation coupling term from the Hamiltonian (26), neglected up to now, grows in importance compared to the $A_{so}\hat{L}\cdot\hat{S}$. The eigenvalues of the Hamiltonian with both \hat{H}_{so} and \hat{H}_{sr} terms are

$$\tilde{v}_{1/2} = B[J(J+1) - \Lambda^2 + 1/4] - \frac{\gamma}{2} \pm \sqrt{(B - \gamma/2)^2 (J+1/2)^2 - \Lambda^2 B A_{so} + (\Lambda A_{so}/2)^2} \quad (92)$$

In the limit $B \gg A_{so}, \gamma$ we obtain from Eq. (92)

$$\tilde{v}_{N=J+1/2} = B[N_{J+1/2}(N_{J+1/2}+1) - \Lambda^2] - \frac{\gamma}{2}(N_{J+1/2}+1) - \frac{\Lambda^2 A_{so}}{2N_{J+1/2}} \quad (93)$$

$$\tilde{v}_{N=J-1/2} = B[N_{J-1/2}(N_{J-1/2}+1) - \Lambda^2] + \frac{\gamma}{2}N - \frac{\Lambda^2 A_{so}}{2(N_{J-1/2}+1)} \quad (94)$$

Thus the contribution of the spin-rotation term (26) to the energy increases linearly with increasing J . These formulae are analogous to their counterparts (78/79) for $^2\Sigma$ electronic states.

b) Hund's case (b)

When the effect of the spin-orbit coupling is small compared to the effect of the rotation, i.e. at $B \gg |A_{SO}|$, the Hamiltonian (25+26+28) is conveniently written in the form

$$\begin{aligned}\hat{H}_R &= H_1 + \hat{H}_2, \\ \hat{H}_1 &= \frac{B}{\hbar^2}(\hat{J}^2 + \hat{S}^2 - \hat{L}_z^2) - \frac{2B}{\hbar^2}(\hat{J}_x\hat{S}_x + \hat{J}_y\hat{S}_y + \hat{J}_z\hat{S}_z) = \frac{B}{\hbar^2}(\hat{J}^2 + \hat{S}^2 - \hat{L}_z^2) - \frac{2B}{\hbar^2}(\hat{J} \cdot \hat{S}), \\ \hat{H}_2 &= \frac{\gamma}{\hbar^2}(\hat{N} \cdot \hat{S}) + \frac{A_{SO}}{\hbar^2}\hat{L}_z\hat{S}_z.\end{aligned}\quad (95)$$

The dominant part of the Hamiltonian, \hat{H}_1 , does not commute with \hat{S}_z and \hat{J}_z , and thus neither Σ nor Ω are near good quantum numbers. However, it commutes with the components of the operator $\hat{N} = \hat{J} - \hat{S}$, and consequently with \hat{N}^2 and thus the quantum numbers N for \hat{N}^2 , and Λ for are nearly good. This case can be conveniently handled e.g. using the formalism of reversed momenta $\hat{J}' (= -\hat{J})$ and $\hat{N}' (= -\hat{N})$. The eigenvalues of the Hamiltonian matrix are the same as in the Hund's basis (a), i.e. they are given by Eq. (92). The basis vectors of the case (b) are related to their case (a) counterparts by the Clebsch-Gordan coefficients.

From the spectroscopic point of view, the coupling scheme in Hund's case (b) can be imagined as consisting of the following two phases: The spatial electronic angular momentum \hat{L} and the angular momentum of the nuclei, \hat{R} , couple first into the spinless total angular momentum \hat{N} . In the second phase \hat{N} couples with the spin momentum \hat{S} in the total angular momentum \hat{J} . Recall that here the projection of the spin on the molecular axis is not a constant of motion and consequently, Ω is not a nearly good quantum number.

In electronic transitions that do not involve two Σ species, beside the P and R branches there is also a Q branch corresponding to the selection rule $\Delta J = 0$. The term values are

$$\tilde{\nu} = \tilde{\nu}_0 + F'(J') - F''(J'') = \tilde{\nu}_0 + B'J(J+1) - B''J(J+1) = \tilde{\nu}_0 + (B' - B'')J(J+1). \quad (96)$$

In electronic transitions which involve orbitally (Π , Δ , ...) and spin (doublet, triplet, ...) electronic species there are several P , Q , and R subbranches.

6.4.2. Experimental results

In another study on aluminum¹⁵⁴ we investigated the wavenumber region from 25000 to 45000 cm^{-1} . The spectrum we obtained was dominated by several broad peaks with hardly

visible structure; the most intense of them extended between 31400 and 32200 cm^{-1} , with the maximum at about 31900 cm^{-1} (Fig. 7). An inspection of the standard molecular data sources, like Refs. 47, 56 and 57 showed that the only electronic band-system involving aluminum in combinations with the other species, like hydrogen and oxygen, which are present in our plasma is the $C^2\Pi \rightarrow X^2\Sigma^+$ transition of AlO appearing in the region 30100–34800 cm^{-1} .⁵⁷ However, the assignment of the observed feature to this transition was a very difficult task because a poor quality of the spectrum and the possibility that the bands of the $A^2\Sigma^+ \rightarrow X^2\Pi$ system of OH, whose presence is usual under given experimental conditions, appear in the same wavelength region. The most prominent band (0–0) of this electronic transition lies around 32500 cm^{-1} .⁵⁷

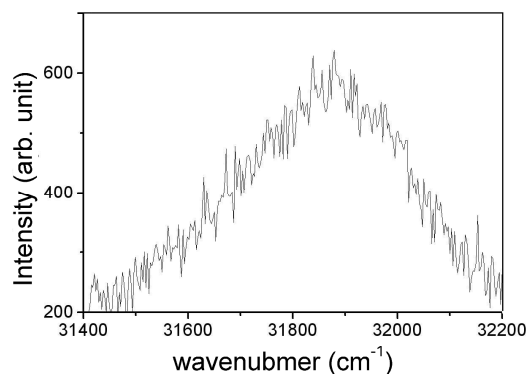


Figure 7.¹⁵⁴ Spectrum between 31400 and 32200 cm^{-1} obtained during PEO of Al.

We found the peak shown in Fig. 7 too broad to be assigned to a single vibrational transition and it seemed to have a richer structure than that expected from a purely vibrational spectrum. In order to identify the structure of this peak, a smoothing procedure based on the Savitzky–Golay method,¹⁵⁵ implemented in the software package ORIGIN, was applied. The results obtained in this way are depicted in Fig. 8.

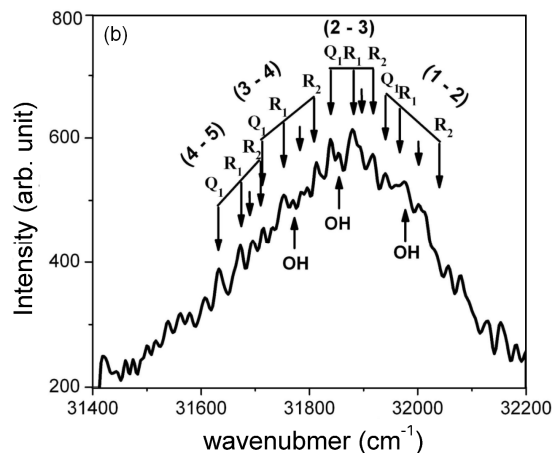


Figure 8. The spectrum obtained after 5-point smoothing of the original data. Thin vertical lines: estimated positions of the AIO branches taken and positions of possible OH bands.

The central question at this stage was whether the structure of the spectrum in Fig. 8 has physical origin or represents artifacts caused by the low signal–noise ratio, limited accuracy of measurements, and/or mathematical manipulation with the experimental results. As a preliminary test, we handled the spectrum of the D₂ lamp in the same way. Though the D₂ spectrum was not completely smooth, it was quite monotonous and the relative intensity of local peaks was by a factor of ten smaller than that in the spectrum of the alumina sample. That seemed to be a strong indication that the structure of the spectrum such as shown in Fig. 8 was not simply caused by statistical noise fluctuations.

In the second step, we carefully checked whether the features of the spectra extracted in this way depended on the choice of the smoothing criterion. We specified the number of points that control the degree of smoothing (“filter width”) from 3 to 9. It turned out that the main consequence of the enlargement of the number of points involved in the smoothing procedure was disappearance of some (smaller) peaks; the positions of those, which did not disappear were in general not significantly changed. It was decided to work further using the smoothing procedure that involves the groups of 5 points to calculate each averaged result.

Another test of reliability of our results was made by carrying out 15 experiments under same conditions. The result of these measurements was the systematic appearance of 16 peaks in the wave number region between 31620 cm⁻¹ and 32040 cm⁻¹. The variation of their positions from one experiment to another remained within the error margin of about 10 cm⁻¹.

As mentioned in the first paragraph of this subsection, we expected in our spectrum the appearance of the AlO and, possibly, OH bands. We carried out an analysis of the reliability of three possibilities: (i) the observed spectrum corresponded to the $A^2\Sigma^+ \rightarrow X^2\Pi$ transition of OH; (ii) it had to be assigned to the $C^2\Pi \rightarrow X^2\Sigma^+$ transition of AlO; (iii) both of these transitions were involved in the spectrum.

(i) The equilibrium bond lengths in the $X^2\Pi$ and $A^2\Sigma^+$ electronic states of OH are 0.96966 and 1.0121 Å, and the vibrational wave numbers are 3738 and 3179 cm^{-1} , respectively.⁵⁶ Using these data, we computed in the harmonic approximation the *FCFs* for transitions between the low-lying vibrational levels of both electronic states in questions. We concluded that the most intense transitions are those with $\nu' = \nu''$, being a consequence of the relatively small change of the internuclear distance (0.042 Å). Because of quite different values of the vibrational fundamentals, the 0–0, 1–1 and 2–2 members of this sequence of bands should be clearly separated from one another. Further, the position of none of the most intense bands of OH is close to the maximum of the recorded spectrum. Thus, although this tentative analysis did not exclude the possibility that the OH bands contribute to the observed spectrum, it seemed to be clear that the spectrum cannot be caused only by this transition.

(ii) The equilibrium bond lengths in the $X^2\Sigma^+$ and $C^2\Pi$ states of AlO are 1.618 and 1.685 Å, and the vibrational fundamentals are 979 cm^{-1} and 856.5 cm^{-1} , respectively.⁵⁶ Using these parameters we computed the *FCFs* for the transitions between the low-lying vibrational levels of the $X^2\Sigma^+$ and $C^2\Pi$ states. Since the electric moment for the transition between these two electronic species does not dramatically vary with the change of the internuclear distance (see Fig. 5 of Ref. 119), the *FCFs* should reliably represent the intensity distributions in the spectrum. In this case, the change of the bond length is significantly larger (0.067 Å) than in the $A^2\Sigma^+ \rightarrow X^2\Pi$ transition of OH. This causes that in general the $\Delta\nu = \pm 1$, and at larger ν values even $\Delta\nu = \pm 2$ transitions are of comparable intensity as their $\Delta\nu = 0$ counterparts. It was even found that the transitions with $\Delta\nu = \pm 1$ should be stronger than those with $\Delta\nu = \pm 0$ (the exception is the 0–0 vibrational transition, being the strongest one when the population of the $\nu = 0$ level in the initial state is the largest one). For this reason the $C^2\Pi \rightarrow X^2\Sigma^+$ transition of AlO should produce a complex spectrum, capable to cover the whole wave number region recorded. Thus, in the following we focused our attention on this system.

6.4.3. Structure of the $C^2\Pi - X^2\Sigma^+$ bands

In contrast to the situation we had when we assigned the bands of the $B^1\Sigma^+ \rightarrow X^1\Sigma^+$ system of MgO and $B^2\Sigma^+ \rightarrow X^2\Sigma^+$ system of AlO, in the present case we did not have the possibility to use the formulae of the type (50). First, we were not able to determine the origins of the bands we recorded. Secondly, the above two spectral systems, involving solely Σ electronic states are quite simple: In the first case ($^1\Sigma^+ \rightarrow ^1\Sigma^+$) one has only one P and one Q branch, and in the second ($^2\Sigma^+ \rightarrow ^2\Sigma^+$) the rotational lines in the sub-branches $J = N \pm 1/2$ practically coincide with one another, because of a very small difference in the spin-rotation constants $\gamma' - \gamma''$.¹³⁵ Thus, one has a single band head and its position with respect to the band origin can be estimated easily. Further, as will be shown below, we recorded the bands that have not been analyzed thus far in high-resolution gas phase experiments. Thus before starting with the assignment, we had to inquire in detail the structure of a $^2\Pi - ^2\Sigma^+$ spectrum.

The rotational energy levels, with incorporated spin-rotation coupling in the $X^2\Sigma^+$ electronic state of AlO are given by the formulae (78) and (79). Since the spin-rotation constant is positive ($\gamma = 51.66$ MHz),¹²² the F_1 ($J = K + 1/2$) sublevels are above their F_2 ($J = K - 1/2$) counterparts. The $X^2\Sigma^+$ state belongs to Hund's (b) case, and thus the F_1 and F_2 levels corresponding to the same K are of the same parity, $(-1)^N$. The energy level schema is presented in Fig. 9, bottom (of course, with exaggerated spin-rotation splitting).

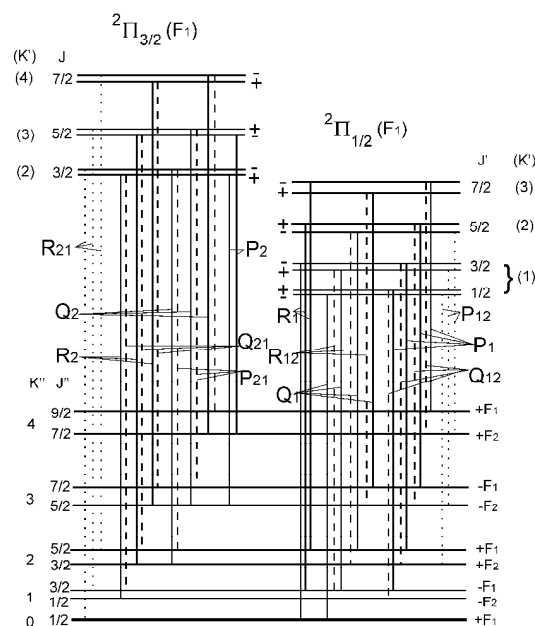


Figure 9. Energy level schema for a band of the $C^2\Pi - X^2\Sigma^+$ system of AlO. The magnitude of the spin-rotation splitting in the $X^2\Sigma^+$ and Λ -splitting in the $C^2\Pi$ are exaggerated, and the energy difference between $^2\Pi_{3/2}$ and $^2\Pi_{1/2}$ components of the $C^2\Pi$ state is diminished.

The $C^2\Pi$ electronic state of AlO belongs to Hund's (a) case, with $|A_{SO}| \gg B$. Since the $^2\Pi$ state in question is of ... π^1 -type, the spin-orbit constant is positive ($A_{SO} = 73.9230 \text{ cm}^{-1}$),¹⁴⁰ i.e. the state is "regular", with the $\Omega = 3/2$ (F_2) sub-state above its $\Omega = 1/2$ (F_1) counterpart. Thus, when speaking about the bands of the $C^2\Pi - X^2\Sigma^+$ system, we may use the terminology $^2\Pi_{3/2} - ^2\Sigma^+$ and $^2\Pi_{1/2} - ^2\Sigma^+$ sub-bands.⁴⁷ If we neglect the spin rotation coupling, in accord with the results presented in ref. 140, the rotation plus spin-orbit structure of the spectrum is determined by Eqs. (90). According to it, the separation between the levels with the same J is in the present approximation (note that we also neglect the dependence of the rotational constant on J) in the $^2\Pi_{3/2} - ^2\Sigma^+$ and $^2\Pi_{1/2} - ^2\Sigma^+$ sub-bands is $A_{SO} - 2B'$. On the other hand, the separation between lowest-lying rotational levels in two $^2\Pi$ sub-states, $J = 3/2$ of the $^2\Pi_{3/2}$ component, and $J = 1/2$ of $^2\Pi_{1/2}$ is $A_{SO} + B'$. The energy schema is shown in Fig 9, top. Additionally, the Λ -type splitting (again exaggeratedly) is indicated. The two Λ -sublevels have opposite parity and ordering of + and - levels is an alternating function of J ,

i.e. the upper sublevel has the $(-1)^{J-1/2}$ parity. Besides, in Fig 9 we label the rotational levels of the $C^2\Pi$ state by (K') , although in Hund's scheme (b) K is not a good quantum number. Note that with increasing J Hund's case (a) tends toward the case (b). A consequence thereof is that the "satellite" branches (with $\Delta J \neq \Delta K$) become less intense.

The selection rules for the rotational transitions are $J'-J'' = -1$ (P branch), 0 (Q branch) and $+1$ (R branch), and $+\leftrightarrow-$ [The near selection rule $N'-N''=0,\pm 1$, being appropriate for Hund's case (b), does not hold in Hund's case (a).]. Thus we have in total twelve branches, P_{nm}, Q_{nm}, R_{nm} , depending on whether the subscript n of the upper level, F_n , and m of the lower level, F_m , is 1 or 2. For the $^2\Pi_{3/2} - ^2\Sigma^+$ sub-band we have thus $P_{11} \equiv P_1$, P_{12} , $Q_{11} \equiv Q_1$, Q_{12} , $R_{11} \equiv R_1$, and R_{12} , whereas for the $^2\Pi_{1/2} - ^2\Sigma^+$ sub-band there are P_{21} , $P_{22} \equiv P_2$, Q_{21} , $Q_{22} \equiv Q_2$, R_{21} , and $R_{22} \equiv R_2$ branches.

Using the rotational constants $B''=0.64136$ ⁴⁷ and $B'=0.600792$ ¹⁴⁰ and the above quoted spin-orbit constant, we computed by means of the formulae (90) (with γ put equal 0) and (69, 70, 96) the Fortrat diagrams presented in Fig. 10. In the approximation applied, the pairs of parabolas P_1 and Q_{12} , Q_1 and R_{12} , Q_2 and P_{21} , R_2 and Q_{21} coincide when drawn as functions of the quantum number J' . For small J values (< 10) these results agree very well with their experimentally derived counterparts presented in Table 1 of Ref. 140; at higher J values slight systematic discrepancies become apparent. All branches are degraded to the red. The branches Q_1/R_{12} , R_1 , R_2/Q_{21} , and R_{21} build heads at $J'=7.5$, 23.5 , 7.5 , and 23.5 , respectively at 2 , 21 , 75 and 94 cm^{-1} with respect to the origin of the $^2\Pi_{1/2}$ sub-state.

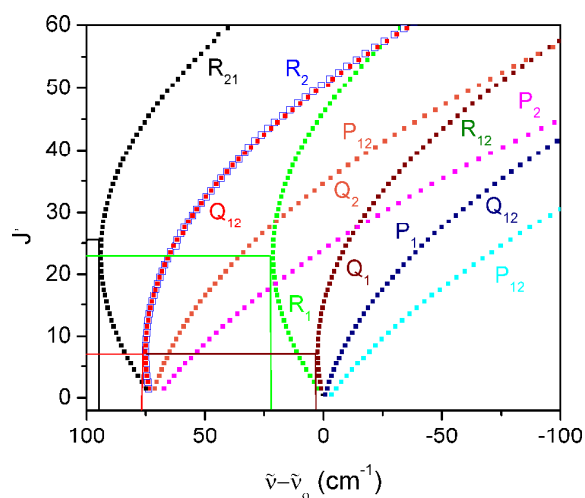


Figure 10. Calculated Fortrat diagrams for the $C^2\Pi - X^2\Sigma^+$ bands.

6.4.4. Identification of bands

The existence of several mutually overlapping branches makes the identification of the bands of the $C^2\Pi \rightarrow X^2\Sigma^+$ transition in AIO quite difficult. In order to solve this problem, we carried out a simulation of the spectrum, based on experimentally observed and assigned band positions. We found most useful the results of an experimental study by Singh and Saksena.¹³⁸ They detected a large number of bands in the region 29000–35000 cm^{-1} and photographed some of them at high resolution. However, the authors were not able to detect all of the expected branches but in most cases only the heads of the Q_1 , R_1 , and R_2 ones. Average wave number differences between the positions of these branches were found to be roughly 30 cm^{-1} ($R_1 - Q_1$) and 50 cm^{-1} ($R_2 - R_1$). These numbers are similar to those we calculated above using the theoretical energy expressions and experimentally derived molecular parameters (about 20 cm^{-1} and 50 cm^{-1} , respectively).

In the present case we refrained from trying to calculate the vibrational levels of the $C^2\Pi$ electronic state. We estimated instead the positions of the Q_1 , R_1 , and R_2 branch heads for all relevant vibrational levels, using the experimental data published by Singh and Saksena.¹³⁸ They are given on the top of Table 10. Combining these numbers with vibrational term values for the $X^2\Sigma^+$ state, we constructed the complete Deslandres table for the $C^2\Pi - X^2\Sigma^+$ spectral system of AIO. The experimental results, where available, are given in parentheses. It can be seen that the results of simulation of the spectrum agree in all cases within few wave numbers with the corresponding experimental findings. This is an indication for the internal consistency and reliable interpretation of the experimental results published in Ref. 138.

Table 10. Simulation of the $C^2\Pi - X^2\Sigma^+$ electronic spectrum of AIO. Vibrational levels of the ground state are calculated by means of Eq. (1). Relative positions of the excited-state levels corresponding to Q_1 , R_1 and R_2 branch heads (three top rows) are estimated on the basis of experimental data from Ref. 138. Transition energies are given in form of a triple Deslandres table – the ordering is from top to bottom Q_1 , R_1 , R_2 , and the wave numbers are labeled by ^c (calculated). The original experimental data from Ref. 138 are given in parentheses. The results of our study are given (right in each column) without parentheses and superscript.

T_v	Q_1	33012 ^c	33862 ^c	34693 ^c	35512 ^c	36322 ^c
	R_1	33045 ^c	33895 ^c	34726 ^c	35545 ^c	36355 ^c
	R_2	33096 ^c	33946 ^c	34777 ^c	35596 ^c	36406
T_v	v	0	1	2	3	4
		33012 ^c	33862 ^c	34693 ^c	35512 ^c	36322 ^c
0 ^c	0	33045 ^c	33895 ^c	34726 ^c	35545 ^c	36355 ^c
		33096 ^c	33946 ^c	34777 ^c	35596 ^c	36406 ^c
		(33096)	(33946)	(34778)		
		32047 ^c	32897 ^c	33728 ^c	34547 ^c	35357 ^c
965 ^c	1	33080 ^c	33930 ^c	33761 ^c	33580 ^c	33390 ^c
		32131 ^c	32981 ^c	33812 ^c	34631 ^c	35441 ^c
		(32131)	(32981)	(33812)		
		31095 ^c	31945 ^c 31945	32776 ^c	33595 ^c	34405 ^c
		(31098)				
1917 ^c	2	31128 ^c	31978 ^c 31972	32809 ^c	33628 ^c	34438 ^c
		31179 ^c	32029 ^c 32034	32860 ^c	33679 ^c	34489 ^c
		(31180)	(32030)			
		30158 ^c	31008 ^c	31839 ^c 31836	32658 ^c	33468 ^c
		(30161)				
2854 ^c	3	30191 ^c	31041 ^c	31872 ^c 31875	32691 ^c	33501 ^c
		30242 ^c	31092 ^c	31923 ^c 31921	32742 ^c	33552 ^c
		(30234)				
		29236 ^c	30086 ^c	30917 ^c	31736 ^c	32546 ^c
			(30087)			
3776 ^c	4	29269 ^c	30119 ^c	30950 ^c	31769 ^c 31767	32579 ^c
			(30117)			
		29320 ^c	30170 ^c	31001 ^c	31820 ^c 31812	32630 ^c
			(30163)			
		28327 ^c	29177 ^c	30008 ^c	30827 ^c	31637 ^c 31632
				(30008)		
4685 ^c	5	28360 ^c	29210 ^c	30041 ^c	30860 ^c	31670 ^c 31667
				(30042)		
		28411 ^c	29261 ^c	30092 ^c	30911 ^c	31721 ^c 31722
				(30092)		
		27432 ^c	28282 ^c	29133 ^c	29932 ^c	30742 ^c
					(29932)	
5580 ^c	6	27465 ^c	28315 ^c	28146 ^c	29965 ^c	30775 ^c
					(29965)	
		27516 ^c	28366 ^c	29197 ^c	30016 ^c	30826 ^c
					(30016)	

		26552 ^c	27402 ^c	28233 ^c	29052 ^c	29862 ^c
6460 ^c	7	26585 ^c	27435 ^c	28266 ^c	29085 ^c	29895 ^c (29894)
		26636 ^c	27486 ^c	28317 ^c	29136 ^c	29946 ^c (29946)

In Ref. 154 we presented the results of 15 experiments carried out under the same conditions. In each case a smoothing involving five points is performed. We identified sub-branches Q_1 , R_1 , and R_2 for the transitions $(\nu', \nu'') = (1,2)$, $(2,3)$, $(3,4)$, and $(4,5)$, as shown in Fig. 8. These results are included in Table 10. To our knowledge, only the $(0,1)$ and $(1,2)$ members of the sequence $\nu' - \nu'' = -1$ have been analyzed in the experiments preceding our study 154. Our results agree within the error margin of 10 cm^{-1} with the corresponding positions of band heads, estimated on the basis of previous experimental data. Thus, we believe that a great part of the spectrum we observed in the region between 31400 and 32200 cm^{-1} belongs to the $\nu' - \nu'' = -1$ sequence of the $C^2\Pi - X^2\Sigma^+$ spectral system of AlO.

Beside the peaks we assign to the Q_1 , R_1 , and R_2 sub-branches of the $C^2\Pi - X^2\Sigma^+$ system of AlO, we identified several features that cannot be incorporated in this scheme. We suppose that they could correspond to the 1-1 transition of the $A^2\Sigma^+ - X^2\Pi$ system of OH, as e.g. feature observed at 31992 cm^{-1} (average values for 15 experiments), being close to the position of the R_2 branch of this OH band at 31986 cm^{-1} .⁵⁷ It is also possible that some of the unassigned spectral features correspond to the heads of the R_{21} sub-branch of the $C^2\Pi - X^2\Sigma^+$ system of AlO (see Fig. 10).

7. CONCLUSIONS

In the present review, we describe a part of our investigations on plasma electrolytic oxidation of light metals and their alloys. We recorded emission spectra in order to get information about the processes that take place in our systems, with the aim to become able to monitor them. Due to inherently stochastic appearance of spectral sources (microdischarge plasmas), poor resolution, usually low intensities, and unfavorable signal/noise ratios, we were not able to carry out the assignment of spectral features, particularly of molecular bands,

solely based on use of standard sources of spectral data. Instead, we had to compare our spectra with those obtained in previous spectroscopic measurements, carried out under completely different conditions and giving the results of substantially different kind. On the other hand, it turned out that the systems we are dealing with can serve as a source of new spectroscopic information in large wavelength regions. For estimation of important parameters, like temperature and electron number density, various plasma diagnostics methods had to be applied. The results of measurements of molecular spectra were combined with quantum-mechanical calculations when the standard approaches failed.

Determination of plasma parameters based on spectral measurement supposes the existence of at least partial thermal equilibrium. It was hardly to expect any kind of thermal equilibrium in the systems like those being the subject of the present review. However, there are a number of indications speaking against this skepticism. First, we have shown that there seems to exist at least local thermal equilibrium for individual degrees of freedom. For example, in our recent study on Zr,²⁷ we determined the plasma temperature of $T = 7500 \pm 1000$ by using 45 Zr I (atomic) lines in the wavelength region between 420 and 516 nm. The fact that the majority of them lay very close to the Boltzmann straight line $\ln I \sim E/k$, represents a strong indication for the existence of the local thermal equilibrium for electronic motions. The above temperature value agrees with those obtained by a number of other authors, who used similar, but also quite different methods for their determination.^{21,22,28,29,156,157} On the other hand, in the present study we demonstrate that the intensity distributions within band sequences of two spectral systems, $B^1\Sigma^+ \rightarrow X^1\Sigma^+$ MgO¹⁰⁴ and $B^2\Sigma^+ \rightarrow X^2\Sigma^+$ of AlO¹⁵² also obeyed the Boltzmann law. The values of $T = 11000\text{K} \pm 2000\text{K}$ in the former, and $T = 8000\text{K} \pm 2000\text{K}$ in the later case, being quite similar to that obtained on the basis of relative intensities of Zr atomic lines, show that it is not excluded that the thermal equilibrium exist between different degree of freedom, too. However, this opens the question why the temperature obtained using the $A^2\Sigma^+ (v'=0) - X^2\Pi$ band system of OH was much lower, $3500\text{K} \pm 500\text{K}$, as obtained in our study on Mg,¹⁵² and $T = 2800\text{K} \pm 500$ in PEO of Zr.²⁷ A possible and even quite probable explanation of this discrepancy can be found in the results of previous investigations on the systems similar to the present one. They have led to the conclusion that the discharge plasma consists of a central core, with the temperature at roughly 7000K ,¹⁵⁶⁻¹⁵⁸ surrounded by lower-temperature (about 3500K) regions.³¹ In terms

of this model, OH is predominantly present in the colder zone, whereas the atoms and ions of the metal investigated, as well as molecules built in plasma-chemical reactions, occupy the high-temperature zone.

Acknowledgements: We thank the Ministry of Education, Science, and Technological Development of the Republic of Serbia for financial support (Projects No. 171035 and 172040).

REFERENCES

- [1] S. Stojadinovic, R. Vasilic, I. Belca, M. Petkovic, B. Kasalica, Z. Nedic and Lj. Zekovic, *Corros. Sci.*, 2010, **52**, 3258.
- [2] M. Petković, S. Stojadinović, R. Vasilčić and Lj. Zeković, *Appl. Surf. Sci.*, 2011, **257**, 10590.
- [3] S. Stojadinović, N. Radić, R. Vasilčić, M. Petković, P. Stefanov, Lj. Zeković and B. Grbić, *Appl. Catal., B*, 2012, **126**, 334.
- [4] L.O. Snizhko, A.L. Yerokhin, A. Pilkington, N.L. Gurevina, D.O. Misnyankin, A. Leyland and A. Matthews, *Electrochim. Acta*, 2004, **49**, 2085–2095.
- [5] S. Stojadinović, R. Vasilčić, M. Petković, I. Belča, B. Kasalica, M. Perić and Lj. Zeković, *Electrochim. Acta*, 2012, **59**, 354.
- [6] H.F. Guo, M.Z. An, H.B. Huo, S. Xu and L.J. Wu, *Appl. Surf. Sci.*, 2006, **252**, 7911.
- [7] F.C. Walsh, C.T.J. Low, R.J.K. Wood, K.T. Stevens, J. Archer, A.R. Poeton and A. Ryder, *Trans. Inst. Met. Finish.*, 2009, **87**, 122.
- [8] J.M. Albella, I. Montero and J.M. Martinez-Duart, *Electrochim. Acta*, 1987, **32**, 255.
- [9] S. Ikonopisov, *Electrochim. Acta*, 1977, **22**, 1077.
- [10] Chen-Jui Liang, “*In-situ Impedance Spectroscopy Studies of the Plasma Electrolytic Oxidation Coating Process*”, PhD Thesis, University of Sheffield, 2013.
- [11] M. Petković, S. Stojadinović, R. Vasilčić, I. Belča, Z. Nedić, B. Kasalica and U.B. Mioč, *Appl. Surf. Sci.*, 2011, **257**, 9555.
- [12] G. Sundararajan and L. Rama Krishna, *Surf. Coat. Technol.*, 2003, **167**, 269.
- [13] B.H. Long, H.H. Wu, B.Y. Long, J.B. Wang, N.D. Wang, X.Y. Lu, Z.S. Jin and Y.Z. Bai, *J. Phys. D: Appl. Phys.*, 2005, **38**, 3491.

- [14] A.L. Yerokhin, L.O. Snizhko, N.L. Gurevina, A. Leyland, A. Pilkington and A. Matthews, *J. Phys. D: Appl. Phys.*, 2003, **36**, 2110.
- [15] A.L. Yerokhin, L.O. Snizhko, N.L. Gurevina, A. Leyland, A. Pilkington and A. Matthews, *Surf. Coat. Technol.*, 2004, **177-178**, 779.
- [16] S. Stojadinović, R. Vasilić, M. Petković and Lj. Zeković, *Surf. Coat. Technol.*, 2011, **206**, 575.
- [17] S. Stojadinović, J. Jovović, M. Petković, R. Vasilić and N. Konjević, *Surf. Coat. Technol.*, 2011, **205**, 5406.
- [18] B. Kasalica, M. Petkovic, I. Belca, S. Stojadinovic and Lj. Zekovic, *Surf. Coat. Technol.*, 2009, **203**, 3000.
- [19] L. Wang, L. Chen, Z. Yan and W. Fu, *Surf. Coat. Tehnol.*, 2010, **205**, 1651.
- [20] L. Wang, W. Fu and L. Chen, *J. Alloys Compd.*, 2011, **509**, 7652.
- [21] J. Jovović, S. Stojadinović, N.M. Šišović and N. Konjević, *Surf. Coat. Tehnol.*, 2011, **206**, 24.
- [22] J. Jovović, S. Stojadinović, N.M. Šišović and N. Konjević, *J. Quant. Spectrosc. Radiat. Transfer*, 2012, **113**, 1928.
- [23] S. Stojadinović, R. Vasilić, M. Petković, I. Belča, B. Kasalica, M. Perić and Lj. Zeković, *Electrochim. Acta*, 2012, **59**, 354.
- [24] S. Stojadinović, R. Vasilić, M. Petković, I. Belča, B. Kasalica and Lj. Zeković, *Electrochem. Commun.*, 2013, **35**, 22.
- [25] S. Stojadinović, R. Vasilić, M. Petković, B. Kasalica, I. Belča, A. Žekić and Lj. Zeković, *Appl. Surf. Sci.*, 2013, **265**, 226.
- [26] S. Stojadinović, R. Vasilić, M. Petković, I. Belča, B. Kasalica, M. Perić and Lj. Zeković, *Electrochim. Acta*, 2012, **79**, 133.
- [27] S. Stojadinović, J. Radić-Perić, R. Vasilić and M. Perić, *Applied Spectroscopy*, 2014, **68**, 161.
- [28] R. O. Hussein, X. Nie, D. O. Northwood, A. Yerokhin and A. Matthews, *J. Phys. D: Appl. Phys.*, 2010, **43**, 105203.
- [29] M.D. Klapkiv, H.M. Nykyforchyn and V.M. Posuvailo, *Mater. Sci.*, 1994, **30**, 333.
- [30] R.O. Hussein, X. Nie and D.O. Northwood, *Surf. Coat. Technol.*, 2010, **205**, 1659.

- [31] C.S. Dunleavy, I. O. Golosnoy, J. A. Curran and T. W. Clyne, *Surf. Coat. Technol.*, 2009, **203**, 3410.
- [32] V.M. Pasuvailo and M.D. Klapkiv, *Materials Science*, 1997, **33**, 383.
- [33] V.M. Pasuvailo, *Materials Science*, 2001, **37**, 677.
- [34] B. Kasalica, I. Belča, S. Stojadinović, M. Sarvan, M. Perić and Lj. Zeković, *J. Phys. Chem. C*, 2007, **111**, 12315.
- [35] S. Stojadinovic, I. Belca, M. Tadic, B. Kasalica, Z. Nedic and Lj. Zekovic, *J. Electroanal. Chem.*, 2008, **619-620**, 125.
- [36] B. Kasalica, S. Stojadinović, I. Belča, M. Sarvan, Lj. Zeković and J. Radić-Perić, *J. Anal. At. Spectrom.*, 2013, **28**, 92.
- [37] B.V. Kasalica, I.D. Belca, S.Đ. Stojadinovic, Lj.D. Zekovic and D. Nikolic, *Appl. Spectrosc.*, 2006, **60**, 1090.
- [38] P.R. Bunker, *Molecular Symmetry and Spectroscopy*, Academic Press, New York, 1979.
- [39] M. Born and J.R. Oppenheimer, *Ann. Phys.*, 1927, **389**, 457.
- [40] J.K.G. Watson, *Mol. Phys.*, 1970, **19**, 465.
- [41] J. Brown, A. Carrington, *Rotational Spectroscopy of Diatomic Molecules*, Cambridge University Press, 2003.
- [42] J.T. Hougen, *J. Chem. Phys.*, 1962, **36**, 519.
- [43] R.N. Zare, *Angular Momentum*, John Willey&Sons, Inc. (1988); V.D. Kleiman, H. Park, R.J. Gordon, R.N. Zare, *Companion to Angular Momentum*, J. Wiley&Sons, Inc., 1998.
- [44] J.H. Van Vleck, *Rev. Mod. Phys.*, 1951, **23**, 213.
- [45] J.M. Brown and B.J. Howard, *Mol. Phys.* 1976, **31**, 1517; 1976, **32**, 1197.
- [46] H. Lefebvre-Brion, R.W. Field, *Perturbations in the Spectra of Diatomic Molecules*, Academic Press, 1986.
- [47] G. Herzberg, *Molecular Spectra and Molecular Structure. I. Spectra of Diatomic Molecules*, D. Van Nostrand Co. Inc., Princeton, New Jersey, 1950.
- [48] A. Messiah, *Quantum Mechanics*, John Willey&Sons, Inc., New York, 1964.
- [49] J.M. Brown, J.T. Hougen, K.P. Huber, J.W.C. Johns, I. Kopp, H. Lefebvre-Brion, A.J. Merer, D.A. Ramsay, J. Rostas and R.N. Zare, *J. Mol. Spectrosc.*, 1975, **55**, 500.
- [50] M. Perić, *Elektroni u molekulima, u Elektron – sto godina od otkrića*, свеска прва, *Elektron i svet oko nas*, М. Курепа (Ед.), Завод за уџбенике и наставна средства, Београд, 1997, 311.

- [51] M. Perić, B. Engels and, *Theoretical spectroscopy of small molecules: Ab initio investigations of vibronic structure, spin-orbit splittings and magnetic hyperfine effects in the electronic spectra of triatomic molecules*, in *Understanding Chemical Reactivity, Vol 13, Quantum Mechanical Electronic Structure Calculations with Chemical Accuracy*, S.R. Langhoff (Ed.), Kluwer Academic, Dordrecht, The Netherlands, 1995, 261.
- [52] R. Ranković, S. Stojadinović, M. Sarvan, B. Kasalica, M. Krmar, J. Radić-Perić and M. Perić, *J. Serb. Chem. Soc.*, 2012, **77**, 1483. *Supplementary material S202*.
- [53] M. Perić, R. Runau, J. Römelt, S.D. Peyerimhoff and R.J. Buenker, *J. Mol. Spectrosc.*, 1979, **78**, 309.
- [54] G. Herzberg, *Molecular Spectra and Molecular Structure II. Infrared and Raman Spectra of Polyatomic Molecules*, Van Nostrand Reinhold Reinhold, New York, 1945.
- [55] G. Herzberg, *Molecular Spectra and Molecular Structure III. Electronic Spectra of Polyatomic Molecules*, Van Nostrand, New York, 1967.
- [56] K. P. Huber, G. Herzberg, *Molecular Spectra and Molecular Structure IV. Constants of Diatomic Molecules*, Van Nostrand Reinhold, New York, 1979.
- [57] R.W.B. Pearse and A.G. Gaydon, *The Identification of Molecular Spectra*, Chapman and Hall, London, 1976.
- [58] P.C. Mahanty, *Phys. Rev.*, 1932, **42**, 609.
- [59] P.C. Mahanty, *Indian J. Phys.*, 1935, **9**, 455.
- [60] A. Lagerqvist and U. Uhler, *Nature*, 1949, **164**, 665.
- [61] A. Lagerqvist, *Ark. Mat. Astr. Fys.*, 1943, **A29**, 1.
- [62] L. Brewer and R.F. Porter, *J. Chem. Phys.*, 1954, **22**, 1867.
- [63] D. Pešić and A.G. Gaydon, *Proc. Phys. Soc.*, 1959, **73**, 244.
- [64] D. Pešić, *Proc. Phys. Soc.*, 1960, **76**, 844.
- [65] L. Brewer, S. Trajmar and R.A. Berg, *Astrophys. J.*, 1962, **135**, 955.
- [66] S. Trajmar and G.E. Ewing, *Astrophys. J.*, 1965, **142**, 77.
- [67] M. Singh, *J. Phys. B*, 1971, **4**, 565.
- [68] M. Singh, *J. Phys. B*, 1973, **6**, 1339.
- [69] M. Singh, *J. Phys. B*, 1973, **6**, 1917.
- [70] T. Ikeda, N.B. Wong, D.O. Harris and R.W. Field, *J. Mol. Spectrosc.*, 1977, **68**, 452.
- [71] B. Bourguignon, J.C. McCombie and J. Rostas, *Chem. Phys. Lett.*, 1985, **113**, 323.
- [72] B. Bourguignon and J. Rostas, *J. Mol. Spectrosc.*, 1991, **146**, 437.

- [73] P.C.F. Ip, K.J. Cross, R.W. Field, J. Rostas, B. Bourguignon and J. McCombie, *J. Mol. Spectrosc.*, 1991, **146**, 409.
- [74] E. Kagi, T. Hirano, S. Takano and K. Kawaguchi, *J. Mol. Spectrosc.*, 1994, **168**, 109.
- [75] P. Mürtz, H. Thümmel, C. Pflzer and W. Urban, *Mol. Phys.*, 1995, **86**, 513.
- [76] J.H. Kim, X.Li, L.S. Wang, H.L. de Clercq, C.A. Fancher, O.C. Thomas, K.H. Bowen, *J. Phys. Chem. A*, 2001, **105**, 5709.
- [77] J.W. Daily, C. Dreyer, A. Abbud-Madrid and M.C. Branch, *J. Mol. Spectrosc.*, 2002, **214**, 111.
- [78] D. Bellert, K.L. Burns, N.T. Van-Oanh, J. Wang and W.H. Breckenridge, *Chem. Phys. Lett.*, 2003, **381**, 381.
- [79] D. Bellert, K.L. Burns, N.T. Van-Oanh, J. Wang and W.H. Breckenridge, *Chem. Phys. Lett.*, 2003, **381**, 725.
- [80] J. Wang, N.T. Van-Oanh, D. Bellert, W.H. Breckenridge, M.A. Gaveau, E. Gloaguen, B. Soep and J.M. Mestdagh, *Chem. Phys. Lett.*, 2004, **392**, 62.
- [81] E. Kagi and K. Kawaguchi, *J. Mol. Struct.*, 2006, **795**, 179.
- [82] J. Wang and W.H. Breckenridge, *J. Chem. Phys.*, 2006, **124**, 124308.
- [83] A. Maatouk, A. Ben Houria, O. Yazidi, N. Jaidane and M. Hochlaf, *J. Chem. Phys.*, 2010, **133**, 144302.
- [84] J. Schamps and H. Lefebvre-Brion, *J. Chem. Phys.*, 1972, **56**, 573.
- [85] S. R. Langhoff, C.W. Bauschlicher, Jr. and H. Partridge, *J. Chem. Phys.*, 1986, **84**, 4474.
- [86] H. Thümmel, R. Klotz and S.D. Peyerimhoff, *Chem. Phys.*, 1989, **129**, 417.
- [87] A.F. Jalbout, *J. Mol. Struct.*, 2002, **618**, 85.
- [88] C.W. Bauschlicher, Jr., D.M. Silver and D.R. Yarkony, *J. Chem. Phys.*, 1980, **73**, 2867.
- [89] C.W. Bauschlicher, Jr., B.H. Lengsfeld III, M.Silver and D.R. Yarkony, *J. Chem. Phys.*, 1981, **74**, 2379.
- [90] C.W. Bauschlicher, Jr., S.R. Langhoff and H. Partridge, *J. Chem. Phys.*, 1994, **101**, 2644.
- [91] C.W. Bauschlicher and H. Partridge, *Chem. Phys. Lett.*, 2001, **342**, 441.
- [92] D.R. Yarkony, *J. Chem. Phys.*, 1988, **89**, 7324.
- [93] R.N. Diffenderfer and D.R. Yarkony, *J. Phys. Chem.*, 1982, **86**, 5098.
- [94] R.N. Diffenderfer, D.R. Yarkony and P.J. Dagdigian, *J. Quant. Spectrosc. Radiat. Transf.*, 1983, **29**, 329.

- [95] B. Huron, J.P. Malrieu and P. Rancurel, *Chem. Phys.*, 1974, **3**, 277.
- [96] H. Thümmel, R. Klotz and S.D. Peyerimhoff, *Chem. Phys.*, 1989, **135**, 229.
- [97] MOLPRO, a package of *ab initio* programs written by H.-J. Werner and P.J. Knowles, Version 2008.1, R. D. Amos, A. Bernhardsson, A. Berning *et al.*
- [98] P.J. Knowles and H.J. Werner, *Chem. Phys. Lett.*, 1985, **115**, 259.
- [99] T.H. Dunning, Jr., *J. Chem. Phys.*, 1989, **90**, 1007.
- [100] Unofficial set from D. Feller for Mg, <https://bse.pnl.gov/bse/portal>.
- [101] H.J. Werner and P.J. Knowles, *J. Chem. Phys.*, 1988, **89**, 5803.
- [102] J. Knowles and H.J. Werner, *Chem. Phys. Lett.*, 1988, **145**, 514.
- [103] A. Lagerqvist and U. Uhler, *Ark. Fys.*, 1949, **1**, 459.
- [104] S. Stojadinović, M. Perić, J. Radić-Perić, R. Vasilić, M. Petković and Lj. Zeković, *Surf. Coat. Technol.*, 2012, **206**, 2905.
- [105] P.N. Ghosh, P.C. Mahanty and B.C. Mukkerjee, *Phys. Rev.*, 1930, **35**, 1491.
- [106] D.S. Pešić, *Proc. Phys. Soc.*, 1964, **83**, 885.
- [107] S.S. Prasad and K. Prasad, 1962, **80**, 311.
- [108] C. de Izarra C, *J. Phys. D: Appl. Phys.*, 2000, **33**, 1697.
- [109] A. Lagerqvist, N.E.L. Nilsson and R.F. Barrow, *Ark. Fys.*, 1957, **12**, 543.
- [110] D.C. Tyte, R.W. Nicholls, *Identification Atlas of Molecular Spectra*, 1, Univ. Western Ontario, 1964.
- [111] S.L.N.G. Krishnamachari, N.A. Narasimham and M. Singh, *Canad. J. Phys.*, 1966, **44**, 2513.
- [112] J.K. McDonald and K.K. Innes, *J. Mol. Spectrosc.*, 1969, **32**, 501.
- [113] M. Singh, *Proc. Indian Acad. Sci. A*, 1973, **71**, 82.
- [114] M. Singh, *J. Phys. B*, 1973, **6**, 521.
- [115] M. Singh and M.K. Saksena, *Proc. Indian Acad. Sci. A*, 1973, **77**, 139.
- [116] V.W. Goodlett and K.K. Innes, *Nature*, 1959, **183**, 243.
- [117] L.B. Knight and W. Weltner, Jr., *J. Chem. Phys.* 1971, **55**, 5066.
- [118] S. Rosenwaks, R.E. Steele and H.P. Broida, *J. Chem. Phys.*, 1975, **63**, 1963.
- [119] C. Zenouda, P. Blottiau, G. Chambaud and P. Rosmus, *J. Mol. Struct. (Theochem)*, 1999, **458**, 61.
- [120] S.J. Bares, M. Haak and J.W. Nibler, *J. Chem. Phys.*, 1985, **82**, 670.
- [121] T. Törring and R. Herrmann, *Mol. Phys.*, 1989, **68**, 1379.

- [122] C. Yamada, E.A. Cohen, M. Fujitake and E. Hirota, *J. Chem. Phys.*, 1990, **92**, 2146.
- [123] M. Goto, S. Takano, S. Yamamoto, H. Ito and S. Saito, *Chem. Phys. Lett.*, 1994, **227**, 287.
- [124] H. Ito and M. Goto, *Chem. Phys. Lett.*, 1994, **227**, 293.
- [125] A. Bernard and R. Gravina, *Z. Naturforsch* 1984, **39a**, 1049.
- [126] M.J. Sayers and J.L. Gole, *J. Chem. Phys.*, 1977, **67**, 5442.
- [127] O. Launila and J. Jonsson, *J. Mol. Spectrosc.*, 1994, **168**, 1.
- [128] O. Launila and L.E. Berg, *J. Mol. Spectrosc.*, 2011, **265**, 10.
- [129] D.M. Lindsay and J.L. Gole, *J. Chem. Phys.*, 1977, **66**, 3886.
- [130] M. Singh, G.V. Zope and S.L.N.G. Krishnamachari, *J. Phys. B: Atom. Mol. Opt. Phys.*, 1985, **18**, 1743.
- [131] J.A. Coxon, S. Naxakis, *J. Mol. Spectrosc.*, 1985, **111**, 102.
- [132] M.D. Saksena, G.S. Ghodgaonkar and M. Singh, *J. Phys. B: Atom Mol. Opt. Phys.*, 1989, **22**, 1993.
- [133] H. Ito, *Can. J. Phys.*, 1994, **72**, 1082.
- [134] N. Sato, H. Ito and K. Kuchitsu, *Chem. Phys. Lett.*, 1995, **240**, 10.
- [135] M.D. Saksena, M.N. Deo, K. Sunanda, S.H. Behere and C.T. Londhe, *J. Mol. Spectrosc.*, 2008, **247**, 47.
- [136] M. Singh and M.D. Saksena, *Can. J. Phys.*, 1981, **59**, 955.
- [137] M. Singh and M.D. Saksena, *Can. J. Phys.*, 1982, **60**, 1730.
- [138] M. Singh and M.D. Saksena, *Can. J. Phys.*, 1983, **61**, 1347.
- [139] M. Singh and M.D. Saksena, *Can. J. Phys.*, 1985, **63**, 1162.
- [140] J.P. Towle, A.M. James, O.L. Boure and B. Simard, *J. Mol. Spectrosc.*, 1994, **163**, 300.
- [141] J.P. Towle, A.M. James, O.L. Boure, B. Simard, M. Singh and M.D. Saksensa, *J. Mol. Spectrosc.*, 1994, **167**, 472.
- [142] S.R. Desai, H. Wu, C.M. Rohlffing and L.S. Wang, *J. Chem. Phys.*, 1997, **106**, 1309.
- [143] S.R. Desai, H. Wu and L.S. Wang, *Int. J. Mass. Spectrom. Ion. Proc.*, 1996, **159**, 75.
- [144] N.V. Joshy, T.K. Mandal and B.L. Jha, *Acta Phys. Pol. A*, 1988, **73**, 613.
- [145] C.T. Londhe, K. Sunanda, M.D. Saksena and S.H. Behere, *J. Mol. Spectrosc.*, 2010, **263**, 178.
- [146] M. Yoshimine, A.D. McLean and B. Liu, *J. Chem. Phys.*, 1973, **58**, 4412.
- [147] G. Das, T. Janis and A.C. Wahl, *J. Chem. Phys.*, 1974, **61**, 1274.

- [148] B.H. Lengsfeld III and B. Liu, *J. Chem. Phys.*, 1982, **77**, 6083.
- [149] J. Schamps, *Chem. Phys.*, 1973, **2** 352.
- [150] V.M. Kovba and I.A. Topol, *J. Mol. Struct. (THEOCHEM)*, 1986, **137**, 65.
- [151] A. Marquez, M.J. Capitan, J.A Odriozola, J.F. Sanz, *Int. J. Quant. Chem.*, 1994, **52**, 1329.
- [152] S. Stojadinović, M. Perić, M. Petković, R. Vasilić, B. Kasalica, I. Belča and J. Radić-Perić, *Electrochim. Acta*, 2011, **56**, 10122.
- [153] B. Rosen, *Phys. Rev.*, 1945, **68**, 124.
- [154] M. Sarvan, M. Perić, Lj. Zeković, S. Stojadinović, I Belča, M. Petković and B. Kasalica, *Spectrochim. Acta A*, 2011, **81**, 672.
- [155] A. Savitzky and M.J.E. Golay, *Anal. Chem.*, 1964, **36**, 1627.
- [156] R.O. Hussein, P. Zhang, X. Nie, Y. Xia and D.O. Northwood, *Surf. Coat. Technol.*, 2011, **206**, 1990.
- [157] M.D. Klapkiv, *Mater. Sci.*, 1995, **31**, 494.
- [158] M.D. Klapkiv, *Mater. Sci.*, 1999, **35**, 279.